Journal of Fluids and Structures 63 (2016) 302–324

Contents lists available at ScienceDirect

Journal of Fluids and Structures

journal homepage: www.elsevier.com/locate/jfs

Two-dimensional wake dynamics behind cylinders with triangular cross-section under incidence angle variation

Zhi Y. Ng, Tony Vo, Wisam K. Hussam, Gregory J. Sheard *

The Sheard Lab, Department of Mechanical and Aerospace Engineering, Monash University, VIC 3800, Australia

ARTICLE INFO

Article history:
Received 8 September 2015
Received in revised form
23 March 2016
Accepted 13 April 2016

Keywords:
Bluff-body
Flow separation
Two-dimensional flows
Triangular cylinder
Vortex streets
Wakes

ABSTRACT

The wakes behind cylinders having an equilateral triangular cross-section are studied numerically for various cylinder inclinations and Reynolds numbers. For steady flows, the development of the recirculation region near the onset of flow separation is described, and the separation Reynolds numbers mapped for different cylinder inclinations. Cylinder inclinations that are not reflection symmetric about the horizontal centreline produce asymmetric recirculation regions which persist until the flow becomes unstable. Flow separation is observed to initiate on the rear-face of the cylinder and develops in size with increasing Reynolds numbers until the separation points become defined at the triangular cross-section's vertices where they remain even at higher Reynolds numbers. Using the Stuart–Landau equation, the critical Reynolds numbers of the different flow cases are quantified. The inclination of the cylinder is seen to strongly affect the location of the separation points, the dimensions of the recirculation region, and ultimately the critical Reynolds numbers. Increasing the Reynolds number past the instability threshold, a Bénard–von Kármán vortex street is initially observed before the downstream region of the wake re-aligns to a bi-layered vortex structure. Beyond this regime, the vortex street is observed to develop variously. At most cylinder inclinations ($\alpha < 30^\circ$ and $\alpha \gtrsim 42^\circ$), the bi-layered wake re-assembles into a secondary vortex street further downstream. For a small range of cylinder inclinations ($30^\circ \leq \alpha \lesssim 38^\circ$), the shedding vortices interact to form a vortex street similar to that produced by the 2P shedding mode for oscillating circular cylinders, while inclinations $38^\circ \lesssim \alpha < 54^\circ$ describe the development of a $P+S$-like vortex street. The formation of these unsteady wakes are attributed to vortex interactions in the wake. The drag and lift force coefficients for various cylinder inclinations and Reynolds numbers are also summarised. Phase trajectories of the force coefficients reveal that the transition from the bi-layered wake to the 2P-like wake alters its profile significantly, while the transitions to the other vortex streets observed did not incur such changes.

1. Introduction

The study of flows past bluff bodies is an ongoing area of immense research interest in fluid mechanics desiring to understand the complexities and underlying dynamics of the emerging flow structures. The wakes trailing these bodies exhibit several known features dependent on the Reynolds number, inducing different force profiles on the body. While

* Corresponding author.
E-mail address: Greg.Sheard@monash.edu (G.J. Sheard).

http://dx.doi.org/10.1016/j.jfluidstructs.2016.04.003
0889-9746/

most wake flow phenomena has been extensively studied for the circular cylinder (Berger and Wille, 1972; Williamson, 1996c), interest in the vortex dynamics of cylinders of prismatic cross-sections have only relatively recently received growing attention. Prismatic cross-section cylinders lack the smooth contours for flow separation that the circular cylinder possesses, and instead presents sharp corners to the flow which alters the flow dynamics. Cylinders with triangular cross-sections in particular find applications in vortex flow meters and turbulence promoters among other applications due to the sharp corners it exhibits, and are also of practical importance in the field of structural design as it models representative geometries. The present study takes a fundamental view to understand the development of these wakes at moderate Reynolds numbers prior to the introduction of complexities from turbulence and chaos.

Studies on the circular cylinder details the following: At low Reynolds numbers, the flow is steady and remains attached to the body. Taneda (1956) verified this experimentally and reported the onset of flow separation to occur at a separation Reynolds number, $Re_s=5$, exceeding which two symmetric recirculation bubbles form at the rear-side of the cylinder. More recently, Sen et al. (2009) utilised finite-element simulations to refine this separation Reynolds number as $Re_s=6.29$, and determined the recirculation length and vorticity to follow Re^1 and $Re^{0.5}$ laws, respectively. At the limit of the steady flow behaviour, the system becomes unstable via a Hopf bifurcation which is well described by the Stuart–Landau equation. The pattern of counter-rotating vortices shed alternately from the cylinder describes the Bénard–von Kármán vortex street, after Bénard (1908) and von Kármán (1911) who observed and studied the stability of the arrangements of the vortices. Jackson (1987) conducted a stability analysis on flows past a circular cylinder and reported the critical Reynolds number as 46, which various other studies found good agreement with (Mathis et al., 1984; Provansal et al., 1987; Sreenivasan et al., 1987). Further investigation into the vortex-shedding process by Perry et al. (1982) found the formation of instantaneous 'alley-ways' in the streamlines of periodic flows penetrating into an otherwise 'closed' cavity observable when the flow is steady. The instantaneous streamlines also reveal the 'centre' and 'saddle' critical points in two-dimensional incompressible flows.

A further instability in the far-wake region of two-dimensional flows has also been observed. Early observations by Taneda (1959) using an aluminium dust visualisation method, and Zdravkovich (1968, 1969) using smoke-visualization techniques elucidated this secondary vortex street. This secondary shedding is reasoned to be the manifestation of a hydrodynamic instability of the mean wake, and appears, initially, as a stationary bi-layered wake which often tends to re-arrange into a street of vortex structures of a larger scale. Durgin and Karlsson (1971), in an experiment subjecting the vortex street to a deceleration, showed that the vortex spacing is crucial to the mode of deformation of the shed vortices, and derived a criterion for eccentricities to develop in the vortices; Karasudani and Funakoshi (1994) later validated this critical vortex spacing value as 0.365 from their experiments using a circular cylinder. Smoke-wire visualizations and measurements conducted by Cimbala et al. (1988) later demonstrated the rapid spatial decay of the Bénard–von Kármán vortex street and the subsequent selective amplification of lower frequency structures in the secondary vortex street. The lower frequency structures were shown to be non-integer factors of the near-wake shedding frequency, and is thus not an instability caused by the amalgamation of the primary vortices. Further studies on the secondary vortex street by Vorobieff et al. (2002), Johnson et al. (2004) and Kumar and Mittal (2012) found the downstream distance of the onset of these structures to agree to a $Re^{-0.5}$ law, and suggests that the development of these vortical structures arise from a convective instability of the time-mean wake.

For other variously shaped bodies, the developing wake region for a two-dimensional flow, while qualitatively similar, exhibits locally different topologies—the presence of eccentricities or sharp edges on a bluff-body alters the flow dynamics sufficiently to give rise to these differences. Jackson (1987) conducted a stability analysis for various cylinder cross-section geometries to determine the effect of geometry on the onset of the periodic flow phenomena, determining the critical Reynolds numbers and corresponding critical Strouhal numbers for the different geometries tested. Sheard et al. (2003), in a study of flows past rings, showed some features of the wake to develop differently than those observed for the canonical circular cylinder where the near wake describes a lack of local symmetry at lower aspect ratios. The separation and critical Reynolds numbers for ellipses of various aspect ratios and inclinations were determined by Paul et al. (2014). A recent study by Thompson et al. (2014) investigating the stability of the wakes of elliptical cylinders showed that the secondary vortex street became increasingly complex with decreasing aspect ratios as the geometry tended to a normal flat plate. They related the behaviour of the increasingly complex vortex street to the circulation per shedding cycle introduced into the wake, the value of which increased with decreasing aspect ratio of the elliptical cylinder. The wakes of square cylinders at incidence have also shown to be an area of considerable interest. Yoon et al. (2010) conducted a parametric study on flows past inclined square cylinders to map the critical Reynolds numbers and different shedding topologies exhibited by the flow as the square cylinder inclination varies from a symmetric to an asymmetric alignment about the horizontal centreline. An investigation on the Re_s value for a square cylinder at zero incidence was conducted by Sen et al. (2011) and showed the initiation of the recirculation region to occur on the rear-face of the cylinder instead of the sharp edges.

Unconfined flows past cylinders with triangular cross-sections, however, have received noticeably less focus despite the geometry featuring sharper corners and stronger asymmetry to the oncoming flow which may alter the dynamics of the flow and the bifurcation scenarios. Most reported works on flows past these prismatic structures only focus on symmetric body orientations where the triangle apex either points directly upstream, or directly downstream. For the cylinder with its apex facing upstream, a stability analysis by Jackson (1987) reported the critical Reynolds number for the onset of unsteady flow to range within 34.318–36.370 for triangle aspect ratios of 0.8 and 1.0, respectively (35.002 by linear interpolation to an equilateral triangle aspect ratio), using a computational domain with a blockage ratio 1/10; while Zielinska and Wesfreid (1995) and De and Dalal (2006), using domains of blockage ratios 1/15 and 1/20, respectively, detailed a global mode

analysis on the velocity distribution of the flows and reported the critical Reynolds number as 38.3 and 39.9, respectively. Zielinska and Wesfreid (1995) also reported that additional simulations on a larger domain with a blockage ratio of 1/40 yielded a higher critical Reynolds number estimate of 39.6. Prhashanna et al. (2011) also reported critical Reynolds numbers of approximately 40.5 and 36.5 for the apex facing upstream and apex facing downstream cases, respectively. Further studies investigating the effects of cylinder inclination variations on the wake dynamics are by Iungo and Buresti (2009) on wind tunnel experiments investigating the aerodynamic forces on finite-span cylinders at $Re_d \approx 1.2 \times 10^5$ (Re_d being the Reynolds number scaled by the cylinder side length d); Bao et al. (2010) on a numerical study reporting the force coefficients at $Re_d = 100$ and 150; and Tu et al. (2014) on characterizing the shedding topology on the cylinder body over a range of Reynolds numbers $50 \leq Re_d \leq 160$. The trends of the force coefficients for increasing cylinder incidence angles reported by Iungo and Buresti (2009) and Bao et al. (2010) were highly similar despite the different Reynolds numbers the investigations were conducted at. In both cases, the highest drag forces were recorded when the triangle apex pointed downstream, and highest lift forces were observed when the triangle base was parallel to the oncoming flow. Variations in the aspect ratio of the triangular cylinder has also been shown to affect the stability of the flow for the cases where the cylinder apex points downstream, but does not affect the onset of the instability significantly when the cylinder apex points upstream (GangaPrasath et al., 2014). More recently Agrwal et al. (2016) conducted experiments at $Re_d = 520$ for the cylinder at several different inclinations, reporting on the wake characteristics. Several other studies on flows past the triangular cylinder have instead focused on the case of a heated cylinder (Zeitoun et al., 2011; Chatterjee and Mondal, 2015).

To the best of the authors' knowledge, an investigation on the development of the wake and its transitions for unconfined two-dimensional flows past cylinders of triangular cross-sections at various inclinations across a range of Reynolds numbers has yet to be reported, thereby motivating the present study. The authors are aware that the flow may become three-dimensional within the range of Reynolds numbers investigated—Luo and Eng (2009) reported for an isosceles triangular cylinder with apex pointing downstream that three-dimensional instability was predicted beyond a Reynolds number of 164 through an instability consistent with Mode A seen behind circular cylinders (Williamson, 1988, 1996b). The stability of the two-dimensional flows at other incidence angles remains unknown, though it undoubtedly will vary at different incidence angles (Sheard et al., 2009; Sheard, 2011). It is paramount therefore that the two-dimensional flows across all incidence angles are properly characterised, which is the main objective of this paper. This investigation further stands to deliver fundamental insight into two-dimensional wake dynamics and secondary wake formation.

This paper is structured as follows: Section 2.1 describes the numerical treatment utilised in this study while Section 2.2 presents data acquired from the grid refinement and domain dependence studies before validating some results against published works. The onset of flow separation, the Hopf bifurcation instability, and vortex shedding and wake patterns at post-critical Reynolds numbers are discussed in Sections 3.1–3.3, respectively. Resulting lift and drag force coefficients for the various wake profiles are reported in Section 3.4, and conclusions are drawn in Section 4.

2. Methodology

The system in this study comprises a cylinder with an equilateral triangular cross-section (hereafter referred to as "cylinder" for brevity) with side length d at incidence α aligned with its axis perpendicular to a uniform freestream flow with velocity U_∞. For this study, α is defined as 0° when the leading vertex of the cylinder points directly upstream, gradually increasing in the counter-clockwise direction to $\alpha = 60°$ when the trailing vertex points directly downstream. Flow solutions for the cylinder at inclinations $\alpha < 0°$ and $\alpha > 60°$ are reflections about the horizontal centreline of the solutions for the cylinder inclined at $0° \leq \alpha \leq 60°$. Fig. 1 shows a schematic of the system described.

The reference length taken for this study is the frontal height h projected by the cylinder towards the oncoming flow. As such, unless mentioned otherwise, the Reynolds number used throughout this study is defined as

$$Re = \frac{U_\infty h}{\nu}, \tag{1}$$

where ν is the kinematic viscosity of the fluid (μ/ρ), μ is the dynamic viscosity, and ρ the fluid density. The cylinder frontal

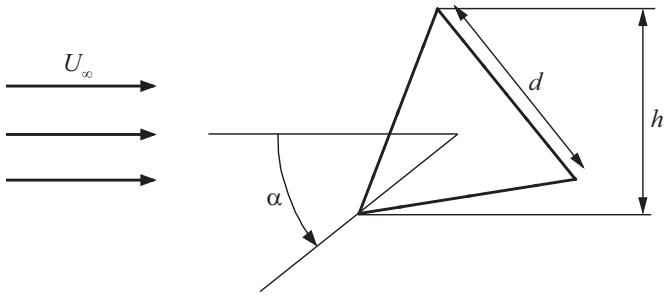

Fig. 1. Geometric properties of the system under investigation.

height h and side length d are related by

$$\frac{h}{d} = \sin(60^\circ - |\alpha - 30^\circ|) + \sin(|\alpha - 30^\circ|), \tag{2}$$

and the Reynolds number based on side length d, Re_d, can be recovered by dividing Eq. (1) by Eq. (2).

2.1. Numerical formulation

The motion of an incompressible fluid is governed by the incompressible Navier–Stokes equations, which, in an inertial frame of reference, is expressed in its normalised form as

$$\frac{\partial \mathbf{u}}{\partial \tau} = -(\mathbf{u}\cdot\nabla)\mathbf{u} - \nabla p + \frac{1}{Re}\nabla^2\mathbf{u}, \tag{3a}$$

$$\nabla\cdot\mathbf{u} = 0, \tag{3b}$$

where the lengths are normalised by the projected frontal height h of the cylinder, the normalised velocities $\mathbf{u}$ are scaled by the freestream velocity U_∞, the non-dimensional time τ is scaled by h/U_∞, and the non-dimensional pressure p is scaled by ρU_∞^2.

The numerical simulation evolves Eq. (3) using a spectral-element method for spatial discretization (Karniadakis and Triantafyllou, 1992) and a third-order accurate time-splitting scheme based on a backward-multistep method (Karniadakis et al., 1991; Blackburn and Sherwin, 2004); wherein the computational domain is subdivided into quadrilateral macro-elements onto which is mapped a Lagrangian tensor-product polynomial shape function. The shape function is interpolated at the Gauss–Legendre–Lobatto quadrature points, enabling the use of the highly efficient quadrature method for integration of the weak form of Eq. (3) which have been recast using the Galerkin method.

The computational domain (example in Fig. 2(a)) is treated with the following boundary conditions: the left edge was assigned a uniform freestream inflow condition while the right edge was given a constant reference pressure and a zero outward normal velocity gradient; the transverse boundaries were treated with a stress-free impermeable boundary condition (slip condition); and imposed on the cylinder surface was a no-slip boundary condition. On all boundaries where a Dirichlet condition was imposed on the velocity field, a suitable Neumann boundary condition was imposed on the outward normal gradient of pressure to preserve the overall third-order time accuracy of the numerical scheme (Karniadakis et al., 1991). The present code has been used and validated in many previous fluid dynamics studies (see Hamid et al., 2015, for various implementations).

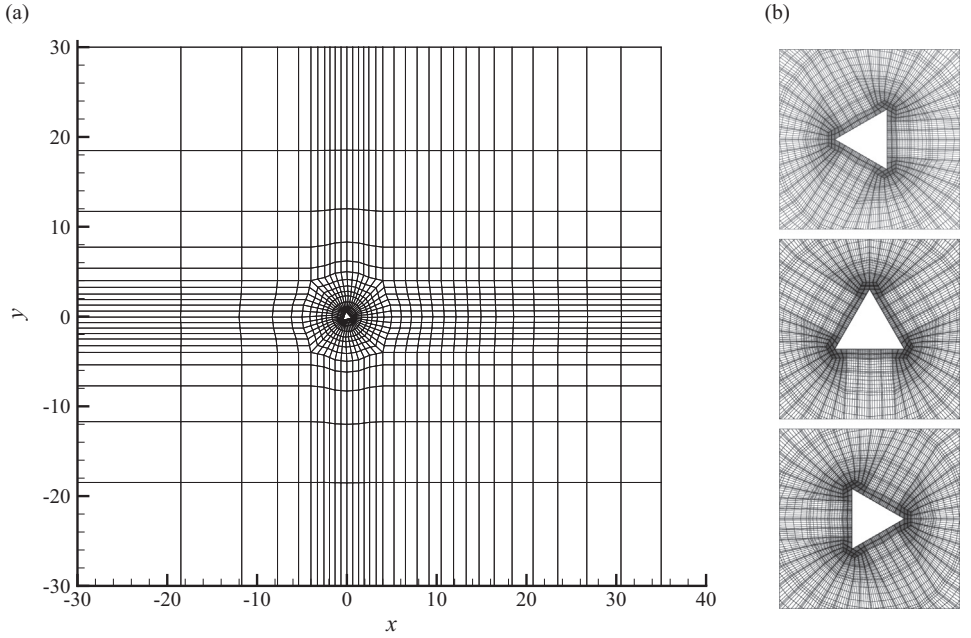

Fig. 2. (a) Final computational domain with the cylinder inclined at $\alpha = 42^\circ$ showing the macro-element distribution. Flow direction is from left to right. (b) Close-up of the cylinder body inclined at (top) $\alpha = 0^\circ$, (middle) $\alpha = 30^\circ$, and (bottom) $\alpha = 60^\circ$ detailing the final interpolation grids in the vicinity of the body.

Table 1
Values of the Strouhal numbers, time-averaged drag and lift force coefficients, and the $\overline{L^2}$ norm as the spatial resolution N^2 is increased. The relative errors (%) to that using an $(N+1)^{\text{th}}$ order polynomial for interpolation are shown in the parentheses.

N^2	5^2	6^2	7^2	8^2	9^2	10^2	11^2
St	0.1702 (0.591%)	0.1692 (0.296%)	0.1687 (0.059%)	0.1686 (0.059%)	0.1685 (0.000%)	0.1685 (0.000%)	0.1685
$\overline{C}_D$	1.9984 (0.035%)	1.9991 (0.040%)	1.9983 (0.050%)	1.9993 (0.005%)	1.9994 (0.000%)	1.9994 (0.045%)	2.0003
$\overline{C}_L$	−1.4875 (0.081%)	−1.4887 (0.175%)	−1.4861 (0.081%)	−1.4873 (0.040%)	−1.4879 (0.040%)	−1.4885 (0.067%)	−1.4895
$\overline{L^2}$ norm	7885.27 (0.086%)	7892.05 (0.097%)	7899.69 (0.021%)	7901.33 (0.011%)	7902.18 (0.002%)	7902.37 (0.000%)	7902.37

2.2. Grid refinement, domain dependence, and validation

Zielinska and Wesfreid (1995), in comparing their results to Jackson (1987), briefly mentioned that the resolution about the sharp edges of the triangular cross-section influences the overall accuracy of the data. Considering the case with $\alpha = 30^\circ$ (largest macro-elements of all incidence angles considered owing to mesh construction) and $Re=200$ (upper bound of Reynolds numbers considered for this study), a grid refinement study was conducted by gradually increasing the order of interpolation of the polynomial shape function N (N^2 nodes per macro-element) to ensure that the dynamics of the flow is adequately resolved. Table 1 shows the results for $5 \le N \le 11$ from the grid resolution study, monitoring the Strouhal numbers St, the time-averaged drag force coefficients $\overline{C}_D$, the time-averaged lift force coefficients $\overline{C}_L$, and the time-averaged integral of the magnitude of velocity (of the saturated flow solution) over the computational domain ($\overline{L^2}$ norm). As characteristic of the spectral-element method, the relative errors decrease exponentially with increasing N^2 values, but at the expense of the permitted time-stepping size. The output parameters from the saturated flow solution obtained using $N=8$ achieves a precision of less than 0.1% to flow solutions obtained using higher N, and shows a close accuracy to the solutions obtained at $N=11$ (the highest N used for this pre-study). This degree of precision and accuracy is likely smaller than the error levels found in corresponding laboratory experiments, and is hence used favourably in proceeding with this study.

The dependence of the flow solutions on the domain size was also investigated to quantify the solution uncertainty arising from the finiteness of the domain. Here, each of the upstream (l_u), downstream (l_d), and transverse (l_{trans}) domain lengths were independently varied from the computational domain size defined ($-30\,h \le x \le 35\,h$ and $-30\,h \le y \le 30\,h$) and evolved to a saturated state using $\alpha = 30^\circ$ and $Re=200$ (same domain size and parameters used for the grid refinement study). The changes in the Strouhal numbers and the time-averaged drag and lift force coefficients were quantified, and the results presented in Table 2. Note that the domain size defined for this study appears to be among the largest compared to previous works on unbounded flows past cylinders with triangular cross-sections. Hence, the final meshes, examples of which are shown in Fig. 2(b), contain 1082 mesh nodes (1016 quadrilateral macro-elements) with an 8^{th} order polynomial shape function imposed through adjoining nodes.

Flows past the cylinder at $\alpha = 0^\circ$ and $\alpha = 60^\circ$ at $Re=100$ were computed to validate the current implementation against the available published data. The results in Table 3 compare well with the most recent study by Wang et al. (2015), where results differed by less than 1% except for the drag force coefficient at $\alpha = 60^\circ$. Presumably, the small discrepancies observed arise from restrictions from the different domain sizes used, and the different numerical methods employed—where the

Table 2
Values of the Strouhal numbers and time-averaged lift and drag force coefficients as the domain lengths were independently varied. The values in the parentheses quantifies the percentage difference (%) of the values relative to M_0.

Mesh	M_0	M_1	M_2	M_3	M_4	M_5	M_6
l_u	$30h$	$10h$	$20h$	$30h$	$30h$	$30h$	$30h$
l_d	$35h$	$35h$	$35h$	$15h$	$25h$	$35h$	$35h$
l_{trans}	$60h$	$60h$	$60h$	$60h$	$60h$	$15h$	$30h$
St	0.1686	0.1738 (3.084%)	0.1694 (0.474%)	0.1626 (3.559%)	0.1672 (0.830%)	0.1729 (2.550%)	0.1702 (0.949%)
$\overline{C}_D$	1.9993	2.0878 (4.427%)	2.0137 (0.720%)	1.9091 (4.512%)	1.9794 (0.995%)	2.1041 (5.242%)	2.0393 (2.001%)
$\overline{C}_L$	−1.4873	−1.5498 (4.202%)	−1.4963 (0.605%)	−1.4118 (5.076%)	−1.4708 (1.109%)	−1.5632 (5.103%)	−1.5167 (1.977%)

Table 3
Comparison of results to published works, all reported for $Re=100$. The values in the parentheses are the relative differences (%) of the results from the present study to available published data.

Source		St	$\overline{C}_D$	C_L'
0°	De and Dalal (2006)	0.1966 (1.02%)	1.7607 (3.21%)	0.2968 (4.31%)
	Wang et al. (2015)	0.196 (0.71%)	1.710 (0.35%)	0.285 (0.35%)
	Present study	0.1946	1.7041	0.2840
60°	Tu et al. (2014)	0.154 (0.71%)	2.122 (3.16%)	0.742 (1.52%)
	Wang et al. (2015)	0.154 (0.71%)	2.097 (2.00%)	0.733 (0.31%)
	Present study	0.1529	2.0550	0.7307

previous studies implemented a finite-element or finite-volume method, the current study utilises a high-order spectral-element technique.

3. Results

Having established the accuracy of the present model, we now proceed to describe the results of the present study.

3.1. Onset of flow separation

The first of the flow states considered is the steady flow at very low Reynolds numbers, with particular interest in understanding the separation of the flow from the body which begins at the separation Reynolds number, Re_s. Several studies have considered this flow state for different cylindrical geometries: flow separation past a circular cylinder initiates at the rear stagnation point, revealing the development of two symmetric counter-rotating recirculation vortices (Taneda, 1956); elliptical cylinders at symmetric cylinder orientations to the incident flow behaves similarly to the circular cylinder, while asymmetric orientations to an oncoming flow shows the inception of a single recirculation vortex on the rear side of the ellipse near the separation Reynolds number (Paul et al., 2014); and the recirculation bubble of flows past rings of certain aspect ratios exhibits a detached recirculation bubble (Sheard et al., 2003).

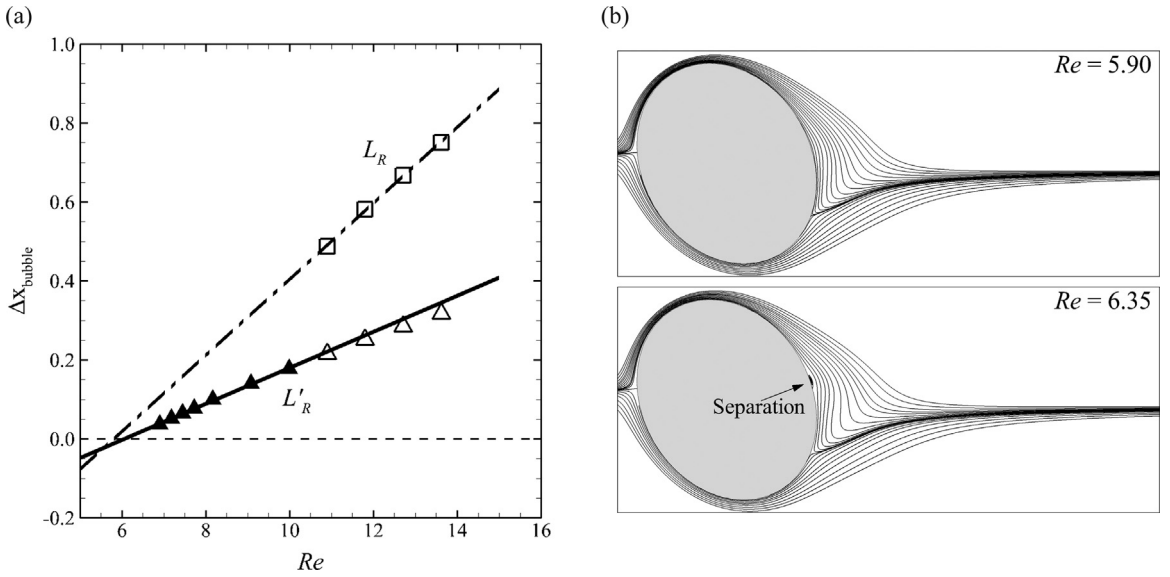

Fig. 3. Flow past an ellipse of aspect ratio 0.8 with its major axis inclined at 60° clockwise to the downstream flow direction. The plots in (a) show L_R' against Re when only a single steady vortex is observed (solid line through ▲), L_R' against Re when the secondary vortex has formed (△), and L_R against Re (– · line through □). Images in (b) are streamlines of the flow for (*top*) $Re=5.90$, and (*bottom*) $Re=6.35$.

At this juncture, we define for this study that we consider a flow to be separated only when a steady recirculation region develops at the rear face of the cylinder to circumvent the possibility of flow separation occurring at the cylinder vertices where the flow faces an intense adverse pressure gradient and may exhibit even a miniscule separation for any finite Reynolds number. The length of the recirculation region, L_R, has in many studies been typically defined as the distance between the rear stagnation point on the cylinder and the wake stagnation point (also the saddle critical point), which coincides with the wake centreline in some previous studies making the measurement of L_R horizontal. The recirculation region has also been shown to develop linearly in length with Reynolds number for variously shaped cylinders, and hence a linear extrapolation of an L_R against Re plot to its intersection on the horizontal axis should yield the separation Reynolds number. However, for flows where separation initiates with a single steady recirculation vortex, the use of L_R becomes invalid as the wake stagnation point remains attached to the cylinder surface. To account for these cases, we propose a modified length measure representative of the recirculation length by using the 'centre' critical point instead – the development of the steady recirculation region showing a saddle point in the steady flow implicates the existence of a 'centre', but with the 'centre' being observable while the saddle point remains on the cylinder surface for the cases with a single recirculation vortex, thus allowing for more flexibility near the onset of separation. Hence, we define a 'recirculation half length' L_R' as the horizontal distance between the 'centre' critical point on a vortex attached to the cylinder body and the rear face of the cylinder and proceed with determining the separation Reynolds numbers in a similar fashion to that using L_R.

To validate L_R' as the length measure, the separation Reynolds number was determined for a test case comprising an ellipse of aspect ratio 0.8 with its major axis inclined at 60° clockwise to the downstream flow direction. This elliptical cylinder geometry was chosen as it is not reflection symmetric about the horizontal centreline and contains a smooth continuous surface for the flow to separate from instead of the sharp corners of the cylinder vertices. The L_R' and L_R measure yielded Re_s values of 6.06 and 5.80, respectively (Fig. 3(a)), meaning that the L_R' -based Re_s estimate is within 4.5% of the estimate based on the conventional L_R measure. The L_R' measure, however, is shown to depart from the linear fit upon the formation of the secondary vortex, and a linear fit through these points results in a separation Reynolds number of 5.64 which underestimates the Re_s value, and a polynomial fit through the L_R' against Reynolds number data predicts a separation Reynolds number of 6.14. The streamlines of the flow (Fig. 3(b)) at $Re=5.90$ (*top*) shows no observable recirculation vortex while the flow at $Re=6.35$ (*bottom*) is separated and shows a single recirculation bubble developing.

Similar to the elliptical cylinder tested, all cylinder inclinations lacking a reflection symmetry about the horizontal centreline (hereafter referred to as "asymmetric cylinder inclinations") marked the onset of flow separation with the inception of a single standing vortex (referred to as the primary vortex in this section) at the rear-side of the cylinder; for

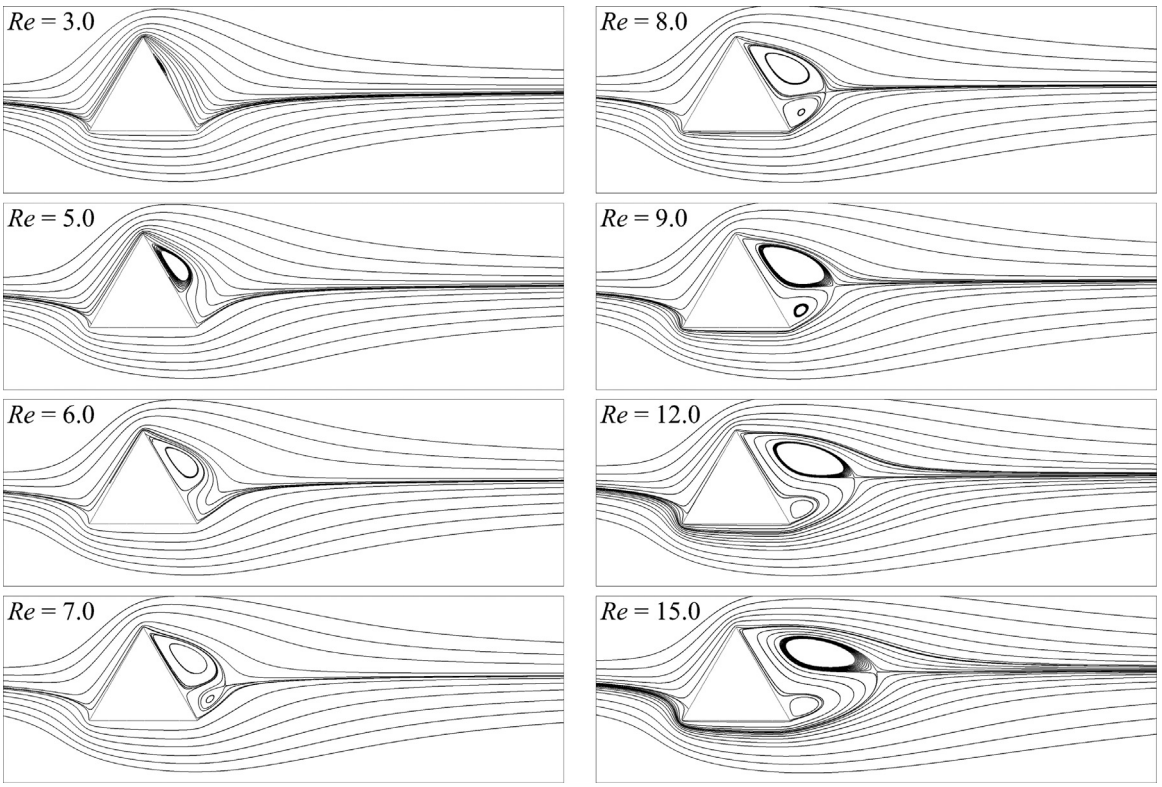

Fig. 4. Streamlines of the separated flow past the cylinder inclined at $\alpha = 30°$. Images from top to bottom then left to right are for $Re=3.0$, 5.0, 6.0, 7.0, 8.0, 9.0, 12.0, and 15.0.

cylinder inclinations with two faces visible from the downstream direction, this primary vortex forms on the face presenting a steeper angle to the streamwise direction. For most cylinder inclinations ($\alpha \lesssim 42^\circ$), as the Reynolds number of the flow is gradually increased, the streamlines of the flow is observed to deflect more intensely over the primary vortex into the wake region, eventually sealing off a region of the flow to form the second recirculation bubble (the secondary vortex). Increasing the Reynolds number further, the secondary vortex is observed to wedge the primary vortex away from the cylinder surface causing it to 'float' in the steady wake. Fig. 4 summarises the scenario of the development of the recirculation region for the cylinder inclined at $\alpha = 30^\circ$ at several Reynolds numbers within $3.0 \leq Re \leq 15.0$. In the figure, the primary vortex is shown to be present through all images (predicted $Re_s = 2.73$), and that the secondary vortex forms only at $6.0 < Re < 7.0$. The primary and secondary vortices are observed to remain attached to the cylinder surface at $Re = 8.0$, and the primary vortex then detaches from the cylinder surface by $Re = 9.0$, initiating the alleyway flow feature. Further increasing the Reynolds number from $Re = 9.0$ to $Re = 15.0$, the alleyway flow feature is observed to increase in width. As this alleyway flow is found to be present in the steady wakes of cylinders lacking a reflective symmetry about the horizontal centreline, not just in the wakes of the triangular cross-section cylinder in this study but in those for bluff rings (Sheard et al., 2003), square cylinders (Yoon et al., 2010), and elliptical cylinders (Park et al., 1989; Paul et al., 2014), it may be deduced that flow fields about any bluff-bodies lacking this reflective symmetry in its geometry will describe a similar asymmetry in its wake. While for circular cylinders the symmetric recirculation bubbles in the 'cavity' flow classically defines the extent of the recirculation, the steady flows past asymmetrically aligned bodies show a mass transfer through the recirculation region of wake.

The formation of the secondary steady vortex at higher cylinder inclinations within $42^\circ < \alpha < 60^\circ$ develop differently to the scenario described above. Here, the secondary vortex that initially forms on the same cylinder surface, according to the scenario described previously for cylinder inclinations outside this range, wedges the primary vortex away from the cylinder surface, causing the secondary vortex to open up into an alleyway flow. The secondary vortex that eventually establishes itself develops over the other cylinder surface due to an increasingly adverse pressure region as the Reynolds number is increased. Fig. 5 elucidates this new scenario for the cylinder inclined at $\alpha = 48^\circ$ where the primary vortex and the initial secondary vortex is shown to have developed by $Re = 10.0$ and the alleyway flow feature to have formed from separating the primary vortex away from the cylinder surface by $Re = 15.0$. Flow separation about the trailing edge of the cylinder is observed at $Re = 20.0$, with the steady secondary vortex being well observed by $Re = 25.0$. In either way the steady secondary vortex develops, a strong similarity to the starting vortices of airfoils in establishing the Kutta condition is observed as both the airfoil and the cylinder here presents a sharp trailing edge.

Interestingly, the symmetric cylinder orientation at $\alpha = 60^\circ$ was the only inclination where symmetric counter-rotating vortices are observed to develop from the onset of separation – the 0° inclination showed flow separation to occur by the scenario described for the asymmetric cylinders but rapidly develops a counter-rotating vortex that is visually symmetrical as expected of symmetric cylinder alignments. To address the question as to whether this occurrence was due to a lack of resolution, the flow with $\alpha = 0^\circ$ was further resolved at an increased resolution of $N^2 = 13^2$, the results showing the same lack of symmetry. While this does not definitively rule out a resolution-dependence on this asymmetry, it strongly supports the conclusion that the asymmetry occurs as a natural feature of the flow. Small localised recirculation regions near the cylinder vertices arising from intense adverse pressure gradients were not observed in any of the results obtained.

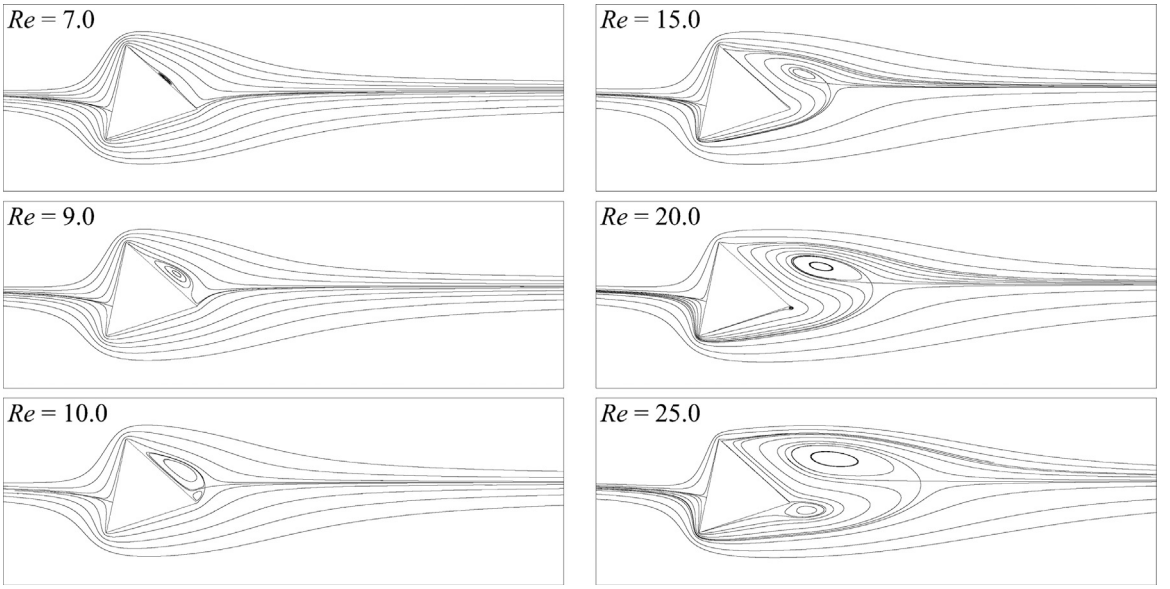

Fig. 5. Streamlines of the separated flow past the cylinder inclined at $\alpha = 48^\circ$. Images from top to bottom then left to right are for $Re = 7.0$, 9.0, 10.0, 15.0, 20.0, and 25.0.

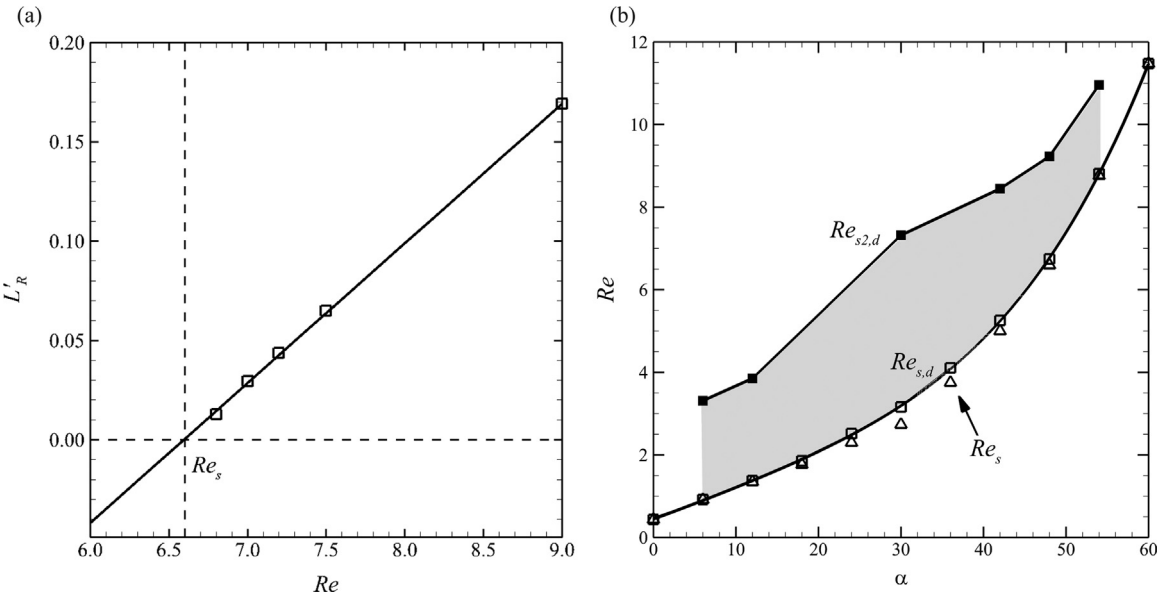

Fig. 6. (a) Plot of L'_R against Re for the cylinder inclined at $\alpha = 48°$. The solid line shows the linear function fitted to predict Re_s and the intersection of the dashed lines marks the threshold for flow separation. (b) Map of the separation Reynolds numbers, Re_s scaled by the cylinder side length d (□) and by the projected height of the cylinder h (△) as the incidence angle α of the cylinder is varied. The solid line through the data of $Re_{s,d}$ is described by Eq. (4). The $Re_{s2,d}$ points (■) approximates the Re_d where the secondary vortex is initially observed.

An example of an L'_R against Re plot used to determine the separation Reynolds numbers is shown in Fig. 6(a), which demonstrates the almost perfectly linear dependence of the two parameters close to the onset of flow separation. Fig. 6(b) summarises the separation Reynolds numbers for the various cylinder inclinations considered, and shows the values to increase monotonically with increasing α. The value of Re_d where the secondary vortex first makes an appearance is approximately mapped for several intermediate cylinder inclinations, shown in Fig. 6(b) as $Re_{s2,d}$. These $Re_{s2,d}$ values for symmetric cylinder inclinations $\alpha = 0°$ and 60° were not determined as the former develops a symmetric wake rapidly past the initial separation while the latter inclination shows the initial separation to manifest with both steady vortices occurring symmetrically; the $Re_{s,d}$ and $Re_{s2,d}$ for both inclinations are equal/approximately equal. Intuitively, the increasing resistance to flow separation for increasing α was expected—the rear faces of the cylinder become less steeply inclined, leading to smaller impulsive decelerations and momentum losses in the flow around the sharp corner and thus also a smaller pressure drop. Increasing the Reynolds number past the onset of separation of the flow from the cylinder, the separation points on the cylinder were observed to move from its point of inception towards the vertices of the cylinder edge where it then remains fixed for any higher Reynolds number. Interestingly, the gradient of the Re_s data for increasing α is non-zero at both $\alpha = 0°$ and 60°, despite the incidence angle smoothly continuing both to $\alpha < 0°$ and $\alpha > 60°$ for redundant inclinations already captured within $0° \le \alpha \le 60°$. Specifically, $\alpha = -1°$ is simply a reflection of $\alpha = 1°$ about the horizontal wake centre-plane, and likewise $\alpha = 61°$ is a reflection of $\alpha = 59°$. Hence over a full 360° range of rotations, Re_s is a non-smooth continuous function of α with differentiability class C^0, with discontinuous gradients every 60° (or when a triangle vertex points directly upstream or downstream).

The gradual trend of the separation Reynolds numbers for the various cylinder inclinations show that a functional relationship may exist, for which a suitable expression is sought. As observed in Fig. 6(b), the data obtained for the separation Reynolds numbers scaled by the cylinder side length d, $Re_{s,d}$, shows a smoother variation than the values scaled by the projected height h particularly at intermediate cylinder inclinations of about $\alpha \approx 30°$. A polynomial function was thus fitted to the $Re_{s,d}$ data to describe this trend, and is presented as Eq. (4) with the corresponding coefficients and goodness-of-fit statistics shown in Table 4.

$$Re_{s,d}(\alpha) = a_0 + a_1\alpha + a_2\alpha^2 + a_3\alpha^3 + a_4\alpha^4. \tag{4}$$

Table 4
(Left) Coefficients of Eq. (4), and (right) the goodness-of-fit statistics of the fitted function. SSE is the sum of squares due to error, R^2 is the coefficient of determination, and $\bar{R}^2$ is the modified coefficient of determination.

a_0	4.45573×10^{-1}		
a_1	7.26661×10^{-2}	SSE	8.32771
a_2	4.75047×10^{-4}	R^2	0.99949
a_3	-1.29131×10^{-5}	$\bar{R}^2$	0.99915
a_4	5.97814×10^{-7}		

Table 5
Values of the separation Reynolds numbers, Re_s, with increasing computational domain sizes. The results for M_0 are for the original domain size used as reported in Fig. 6. The values in the parentheses quantifies the percentage difference (%) of the values relative to the results for DS_3.

α	M_0	DS_1	DS_2	DS_3
0°	0.434 (1.139%)	0.436 (0.683%)	0.438 (0.228%)	0.439
60°	11.503 (0.527%)	11.544 (0.173%)	11.560 (0.035%)	11.564

Several prior studies on the circular cylinder have shown that the size of the computational domain used affects the reliability of the results when modelling the unconfined flow condition, particularly on the evaluation of the force coefficients (Lange et al., 1998; Kumar and Mittal, 2006; Posdziech and Grundmann, 2007; Sen et al., 2009). In these studies, it is noted that the results appear to be increasingly affected at lower Reynolds numbers for a given computational domain. It then becomes essential to obtain an estimate of these domain-related uncertainties for the results of Re_s reported in this paper. While the domain dependence study in Section 2.2 has quantified the associated errors using a test case of $Re=200$, the domain study here focuses on the steady flow regime and bears importance to the credibility of the results in this section. Similar to Posdziech and Grundmann (2007), the initial mesh resolution was retained while the extent of the computational domain was increased by adding additional elements around it to reach the desired domain length. Three square computational domains of dimensions $DS_1 = (100\,h)^2$, $DS_2 = (200\,h)^2$ and $DS_3 = (300\,h)^2$ with the cylinder placed centrally were used to predict the Re_s values for $\alpha=0°$ and 60° (extremes of the Re_s curve shown in Fig. 6), and the uncertainties of each case quantified relative to the results of Re_s for DS_3. The results (provided in Table 5) show little variation in the Re_s values predicted, being approximately 1.1% at worst.

3.2. Transition from steady to time-dependent flow

The first instability in the flow occurs at a critical Reynolds number above which the flow past the body becomes oscillatory in nature. This instability is of a Hopf type and the evolution of the equivalent instability in other bluff body wake flows has been shown to be well-described by the Stuart–Landau equation, which describes the non-linear behaviour of a perturbation about the transition (Provansal et al., 1987; Sreenivasan et al., 1987; Sohankar et al., 1998; Sheard et al., 2004; Paul et al., 2014). Briefly, following Provansal et al. (1987) and Sheard et al. (2004), the Stuart–Landau equation is written as

$$\frac{dA}{d\tau} = (\sigma + i\omega)A - l(1 + ic)|A|^2A + \ldots, \tag{5}$$

where A is the complex mode amplitude ($A = |A|e^{i\Phi}$), $|A|$ the signal magnitude, Φ the phase of the mode, σ is the infinitesimal growth rate, l and c are coefficients describing the non-linear departure of the mode evolution from the linear regime, and ω the angular frequency of the signal in the linear regime; can be decomposed into its real and complex components as

$$\frac{d(\log|A|)}{d\tau} = (\sigma - l|A|^2) + \cdots, \tag{6a}$$

$$\frac{d\Phi}{d\tau} = (\omega - lc|A|^2) + \cdots. \tag{6b}$$

For supercritical bifurcations ($l > 0$), the first two terms of Eq. (6a) (which considers only the real components of the decomposed Eq. (5)) should sufficiently describe the transition behaviour near the onset of the instability. $d(\log|A|)/d\tau$ against

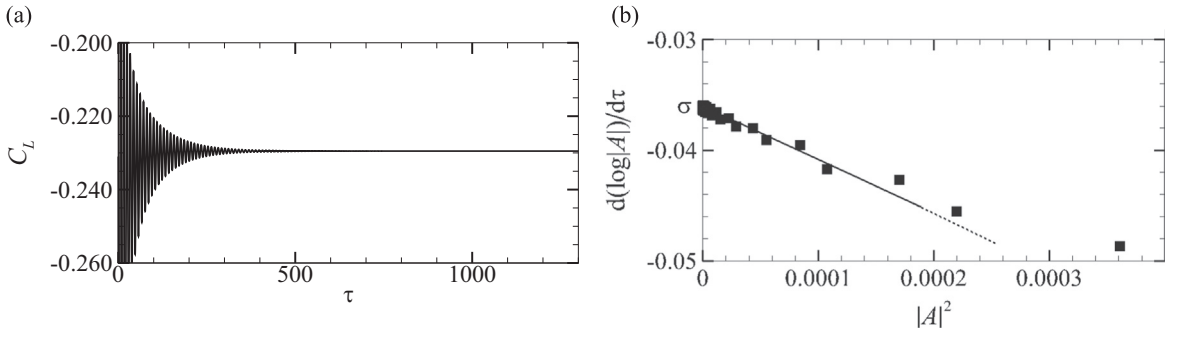

Fig. 7. Typical plots of (a) the transient lift force signal where $\tau=0$ corresponds to the instant the Reynolds number was reduced and (b) the variation of $d(\log|A|)/d\tau$ against $|A|^2$. The plots provided are examples using $\alpha = 48°$.

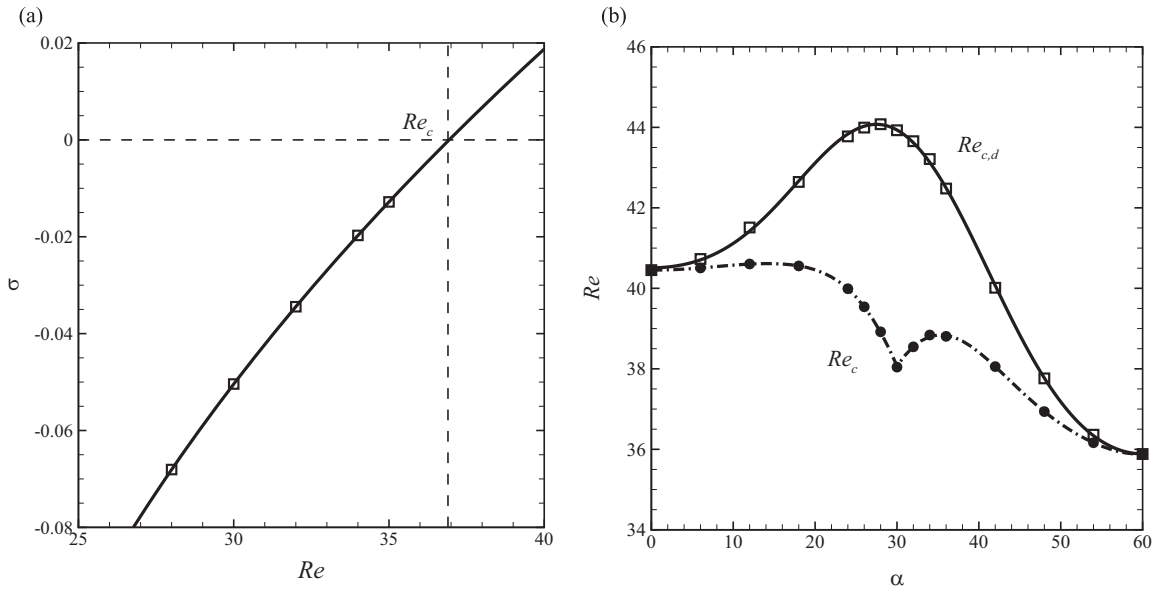

Fig. 8. (a) Typical plot of the infinitesimal growth rates against Reynolds numbers, here shown for $\alpha = 48°$. The solid line describes the fitted inverse polynomial function while the thin dotted lines locate the zero growth rate threshold for the onset of the instability. (b) Plot of the critical Reynolds numbers scaled by the projected frontal height h (●) and by cylinder side length d (□) as a function of the cylinder inclination. The solid line is described by the fitted Fourier function (Eq. (7)) and the dash-dotted line describes Eq. (7) re-scaled to the frontal height h.

$|A|^2$ should thus relate linearly and intercept the vertical axis at the signal growth rate σ. Gathering σ at several Reynolds numbers, and extrapolating to a zero growth rate yields the critical Reynolds number, Re_c. Strictly speaking, the validity of the analysis described above applies only to Reynolds numbers close to the instability threshold. The approach taken for this analysis was to impulsively decay a base flow (evolved to saturation at a Reynolds number exhibiting unsteady flow) to obtain the growth rate of its lift force signal (example in Fig. 7(a)) which was subsequently used to obtain the critical Reynolds number (Sohankar et al., 1998; Thompson and Le Gal, 2004; Yoon et al., 2010; Hussam et al., 2011). The base flows were at $Re = 50$ for all cylinder inclinations, which was chosen from a set of initial simulations as the critical Reynolds numbers were not known *a priori*. It was observed for all cases that the data obtained for the growth rates at various Reynolds numbers (example shown in Fig. 8(a)) did not adhere precisely to a linear profile as was reported in previous studies (Provansal et al., 1987; Sreenivasan et al., 1987). To facilitate better estimations of the critical Reynolds numbers, an inverse polynomial function was fitted to the data for the extrapolation. The decay of the base flow was confined within $0 < Re_c - Re \leq 10$ to ensure the validity of the analysis used (Sohankar et al., 1998).

A plot of the critical Reynolds numbers against α is shown in Fig. 8(b). The cylinder inclined at $\alpha = 0°$ yields a critical Reynolds number of 40.45, which compares well to previously published values of 39.9 (De and Dalal, 2006), 39.6 Zielinska and Wesfreid (1995), and approximately 40.4 (Prhashanna et al., 2011). A discontinuity in the gradient is observed at $\alpha = 30°$, corresponding to when a triangle vertex is pointing vertically upward. This discontinuity arises from the $|\alpha - 30°|$ in the h/d mapping function described by Eq. (2). Interestingly, no such non-smoothness is seen when Re_c is rescaled by the side length d to $Re_{c,d}$. This smoothness, combined with the property that the data over $60° \leq \alpha \leq 120°$ will be a reflection of the data over $0° \leq \alpha \leq 60°$ invites the use of a Fourier series to describe the data. The fitted function is shown in Eq. (7) with its corresponding coefficient values and the goodness-of-fit statistics presented in Table 6, and recovers the original data to within 0.2% of $Re_{c,d}$. The function describing the Re_c data for increasing cylinder inclinations can then be obtained by multiplying Eq. (7) by Eq. (2).

$$Re_{c,d}(\alpha) = \sum_{i=0}^{i=4} a_i \cos\left(i\frac{\pi}{60}\alpha\right). \tag{7}$$

Table 6
(Left) Coefficients of Eq. (7) and (right) the goodness-of-fit statistics of the fitted function. Here χ^2 is the standard chi-square goodness of fit test.

a_0	4.07437×10^1		
a_1	2.27251×10^0	SSE	0.02939
a_2	-2.86780×10^0	R^2	0.99973
a_3	3.90843×10^{-2}	χ^2	0.02939
a_4	3.22403×10^{-1}		

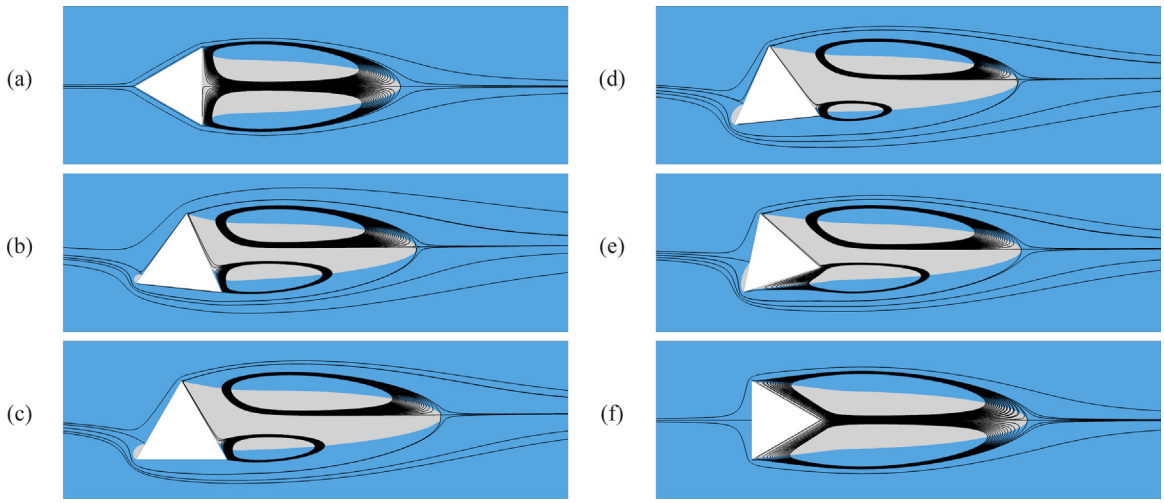

Fig. 9. Streamlines of the steady flow at $Re=35$ for the cylinder inclined at: (a) 0°, (b) 24°, (c) 30°, (d) 36°, (e) 48°, and (f) 60°. The light and dark regions denote negative and positive streamwise velocities, respectively.

As observed in Fig. 8(b), the cylinder inclined at $\alpha \approx 28°$ showed the highest $Re_{c,d}$ value, and the lowest being found at $\alpha = 60°$. A simple explanation for the peak $Re_{c,d}$ value is that the cylinder inclined at $\alpha \approx 30°$ presents the smallest frontal height h to the oncoming flow compared to the other cylinder inclinations, making it more stable as it is a 'smaller' geometry and has a smaller effective Reynolds number. The Re_c curve, however, seems to describe several interesting underlying trends. Re_c is almost independent of cylinder inclination over $0° \leq \alpha \lesssim 18°$, but produces a strong dip in the critical Reynolds numbers for $18° \lesssim \alpha \leq 30°$. Over both of these inclination ranges, the cylinder presents a single surface of the cylinder to the downstream flow. Observations of the pre-critical flows at $Re=35$ at these cylinder inclinations (Fig. 9(a–c)) show the recirculation region forming only over this single side, limiting the width of the wakes produced (and thus also the wake length), justifying the similar critical Reynolds numbers obtained for cylinder inclinations $0° \leq \alpha \lesssim 18°$. The drop in the critical Reynolds numbers for the cylinder inclined at $18° \lesssim \alpha \leq 30°$ is caused by the inception of a small negative streamwise velocity bubble on the steeper leading edge of the cylinder which disturbs the impinging flow making these cases more susceptible to the instability (visible in Fig. 9(b,c)). Over $30° < \alpha \leq 60°$, the cylinder presents two sides of the cylinder to the downstream flow, and demonstrates a small critical Reynolds number peak to occur at $\alpha \approx 34°$. The

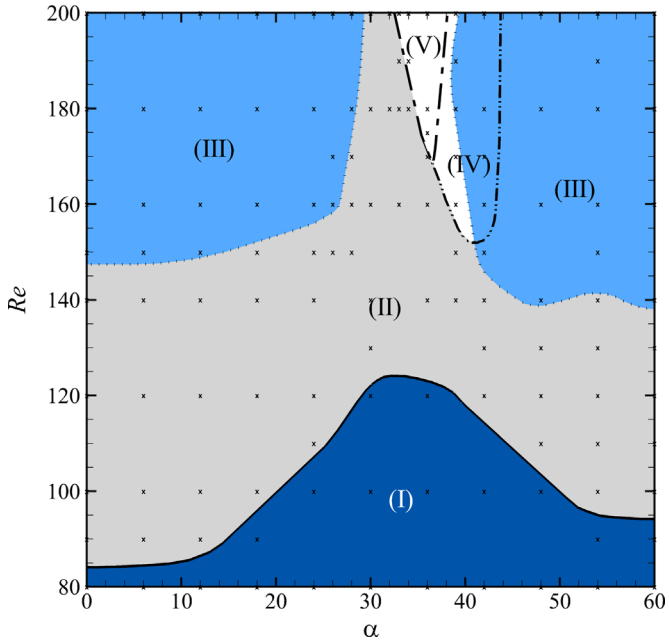

Fig. 10. Map of the different vortex streets exhibited by the unsteady flow. Regime (I) describes the Bénard–von Kármán vortex street, (II) shows the bi-layered wake arrangement, (III) bounded by the dotted line shows the secondary vortex street, (IV) bounded by the (−···) line observes the $P+S$-like wake, and (V) bounded by the (– ·) shows the 2P-like wake. Saturated solutions obtained for this map are dotted in.

difference between the two sides of this peak is that over cylinder inclinations $30^\circ < \alpha \lesssim 34^\circ$, the recirculation region develops over a single side of the cylinder, while the recirculation region of the cylinder at inclinations of $34^\circ \lesssim \alpha \leq 60^\circ$ develops over the two downstream facing sides of the cylinder (see Fig. 9(e,f)) as explained in Section 3.1. The wakes produced from the former inclination range are thus restricted to a smaller width compared to the latter range of incidences which expands over both downstream facing edges of the cylinder.

3.3. *Vortex street variations in the unsteady flow regime*

For cylinders with triangular cross-section, Tu et al. (2014) characterised the topological features of the flow shedding from the cylinder to either be via a main separation pattern (MS), single secondary vortex pattern (SSV), or a vortex merging pattern (VM), with clear descriptions of these patterns provided by Yoon et al. (2010). This part of the present study focuses instead on the structure of the vortex street and the characteristics of the wake. A map of the different vortex streets observed for the various cylinder inclinations and Reynolds numbers tested is provided in Fig. 10. The different wakes observed broadly implies the MS, SSV, and VM shedding patterns affect the structure of the vortex streets produced.

All cylinder inclinations initially exhibit the Bénard–von Kármán vortex street showing an orderly array of counter-rotating vortices alternately shed into the wake. This is Regime (I) in the map presented in Fig. 10, which extends from Re_c (see Fig. 8(b)) up to the onset of regime (II) at a Reynolds number within $80 < Re < 90$ at $\alpha = 0^\circ$ through a Reynolds number within $120 < Re < 130$ at $\alpha \approx 30^\circ$, and retreating to $90 < Re < 100$ at $\alpha = 60^\circ$. At sufficient Reynolds numbers, the advecting vortices at some distance downstream of the cylinder begin to deform and eventually aligns into a bi-layered wake, identified as Regime (II) in Fig. 10. This regime is similar to the scenario described by Durgin and Karlsson (1971) who showed that the vortices deform exceeding a critical vortex spacing ratio. The downstream position of the alignment of the vortices decreases closer towards the cylinder as the Reynolds number is increased. Further increases in the Reynolds number for most cylinder inclinations observes the bi-layered wake to re-arrange itself into a vortex street of a larger scale: the secondary vortex street (Regime III). The onset of these larger-scale vortical structures, first reported by Taneda (1959), introduce incommensurate frequencies into the wake for reasons other than the merging of primary vortices (Cimbala et al., 1988). An example of the development of the vortex street from Regime I through to Regime III is shown in Fig. 11, which will soon be discussed in further detail. For the vortex street observed in Regime IV (bottom two frames in Fig. 12(right)), the cross-wake vortex spacing appears to be much larger than those in Regime I and Regime II, fully separating the dual rows of opposite-signed vortices. A distinctive feature of this regime is the presence of a small single vortex 'riding' along one of the rows of vortices in the wake. The vortex street in Regime IV is also observed to be susceptible to developing a meandering profile in the downstream regions of the wake. In Regime V, the vortex street describes an appearance periodic to two pairs of counter-rotating vortices shed into the wake (bottom frame in Fig. 12(left)). This vortex street features pairs of opposite-signed vortices (not those shed successively but from every alternate pair) to propel away from the wake centreline. As the appearance of the vortex streets observed in Regime IV and Regime V in the figure show a visual similarity to the $P+S$ and

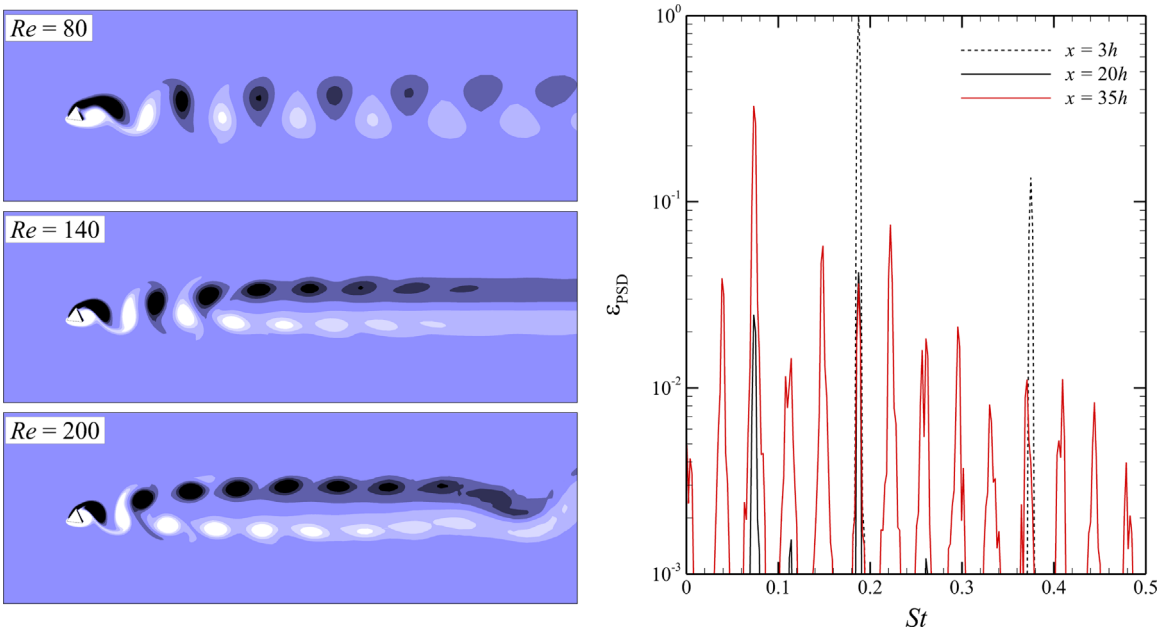

Fig. 11. (Left) Flows past the cylinder inclined at $\alpha = 24^\circ$ at Reynolds numbers Re=80 (I), 140 (II), and 200 (III) from top to bottom, with the corresponding wake regimes indicated in the parentheses. Dark and light shading denote negative and positive vorticities, respectively. (Right) Spectral densities of the transverse velocity signals at positions x=3 h, 20 h, and 35 h describing the frequencies of the wake as it decays.

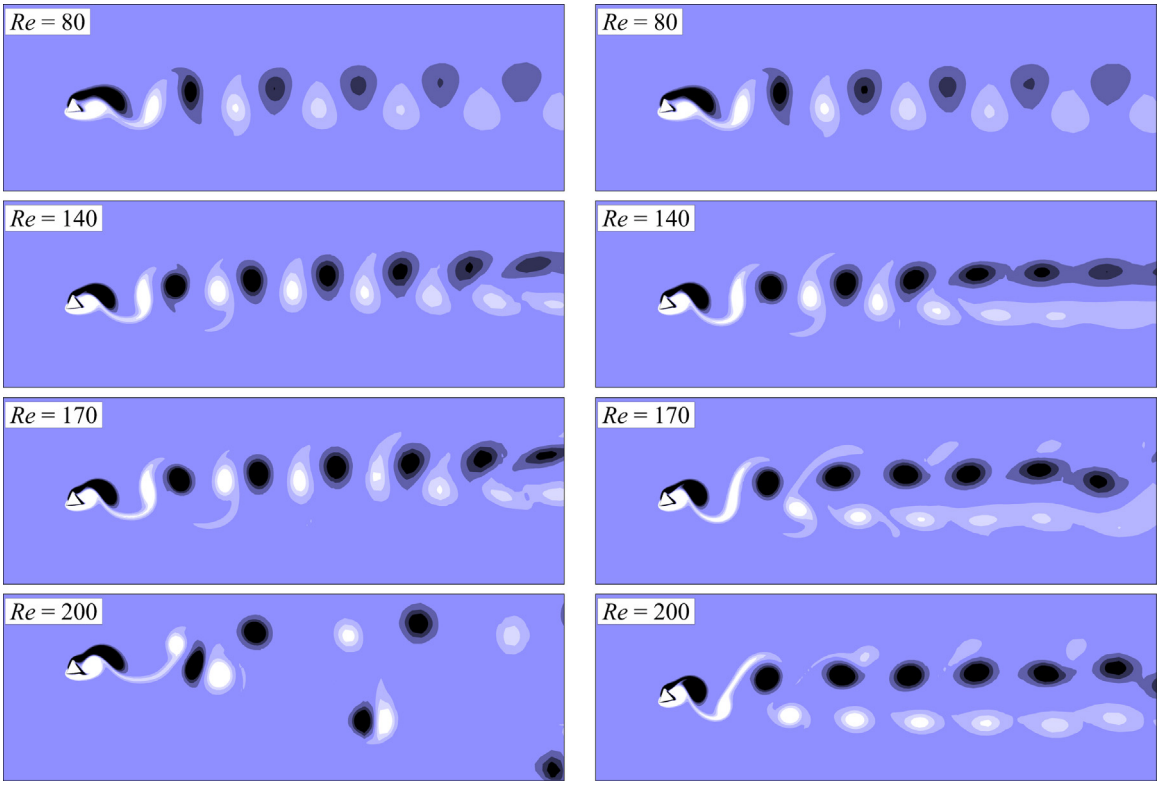

Fig. 12. Flows past the cylinder inclined at (left) $\alpha = 36^\circ$ and (right) $\alpha = 42^\circ$ for Reynolds numbers $Re = 80$, 140, 170, and 200 from top to bottom. For the sequence on the left, the regimes traversed correspond to Regimes I, II, II, and V, while the sequence of the regimes on the right correspond to Regimes I, II, IV, and IV. Dark and light shading denote negative and positive vorticities, respectively.

the 2P shedding modes of the oscillating circular cylinder (Williamson and Roshko, 1988), these regimes are referred to as the $P+S$-like and 2P-like modes. The difference between these modes observed in this study and those for the oscillating cylinder will be discussed.

Fig. 11 describes the development of the wake for the cylinder inclined at $\alpha = 24^\circ$. In the figure (from top to bottom), the Bénard–von Kármán vortex street (Regime I in Fig. 10) is clearly observed for the flow at $Re = 80$. The flow at $Re = 140$ in the middle frame then shows the vortices to have developed spatially into the dual-layered wake (Regime II in Fig. 10), while the secondary vortex street (Regime III in Fig. 10) is clearly observed to develop far downstream in the final frame. The onset of the bi-layered wake profile and the secondary vortex street may possibly be observed at lower Reynolds numbers than predicted as its formation is spatially dependent, and may develop further downstream than the computational domain extent.

Thorough examination of the frequency spectra and velocity distribution in the far wake of the circular cylinder by Cimbala et al. (1988) have described the rapid de-amplification of the dominant Kármán shedding frequency as the vortices traverse further downstream, and the subsequent growth of a broad spectrum of incommensurate frequencies. To determine whether the evolution of the spatial frequency response of the wake of the cylinder geometry in this study agrees well with that reported by Cimbala et al. (1988), a spectral analysis of the transverse velocity signal at 5 positions in the wake of the cylinder ($x = 3$ h, 9 h, 20 h, 30 h, and 35 h) inclined at $\alpha = 24^\circ$ was performed. The spectral density for the flow at $Re = 200$ (shown in Fig. 11 for positions $x = 3$ h, 20 h, and 35 h, and amplitudes normalised by the dominant spectral peak observed in position $x = 3$ h) demonstrates that a similar scenario unfolds for the cylinder geometry in this study—the Kármán shedding frequency with a Strouhal number of approximately 0.187 dominates the near wake along with its associated harmonics but rapidly decays to less than 5% of the initial strength by $x = 20$ h where the bi-layered wake is observed. The velocity signals measured at $x = 30$ h and 35 h where the secondary vortex street has formed shows multiple spectral peaks of comparable strengths over a large frequency band and are non-harmonic. The spectral densities of the flow at $Re = 80$ and 140 (not shown) both show a similar decay of the dominant shedding mode, with the latter decaying at a higher rate.

The wakes of flows past the cylinder inclined at $30^\circ \leq \alpha < 38^\circ$ and $38^\circ < \alpha \lesssim 48^\circ$, however, develop differently to the scenario described for the other cylinder inclinations. The vortex streets produced at these cylinder inclinations are reminiscent of those found for the oscillating circular cylinder (Williamson and Roshko, 1988) despite the cylinder in the present study being stationary. For cylinder inclinations $30^\circ \leq \alpha < 38^\circ$, increasing the Reynolds number from where the

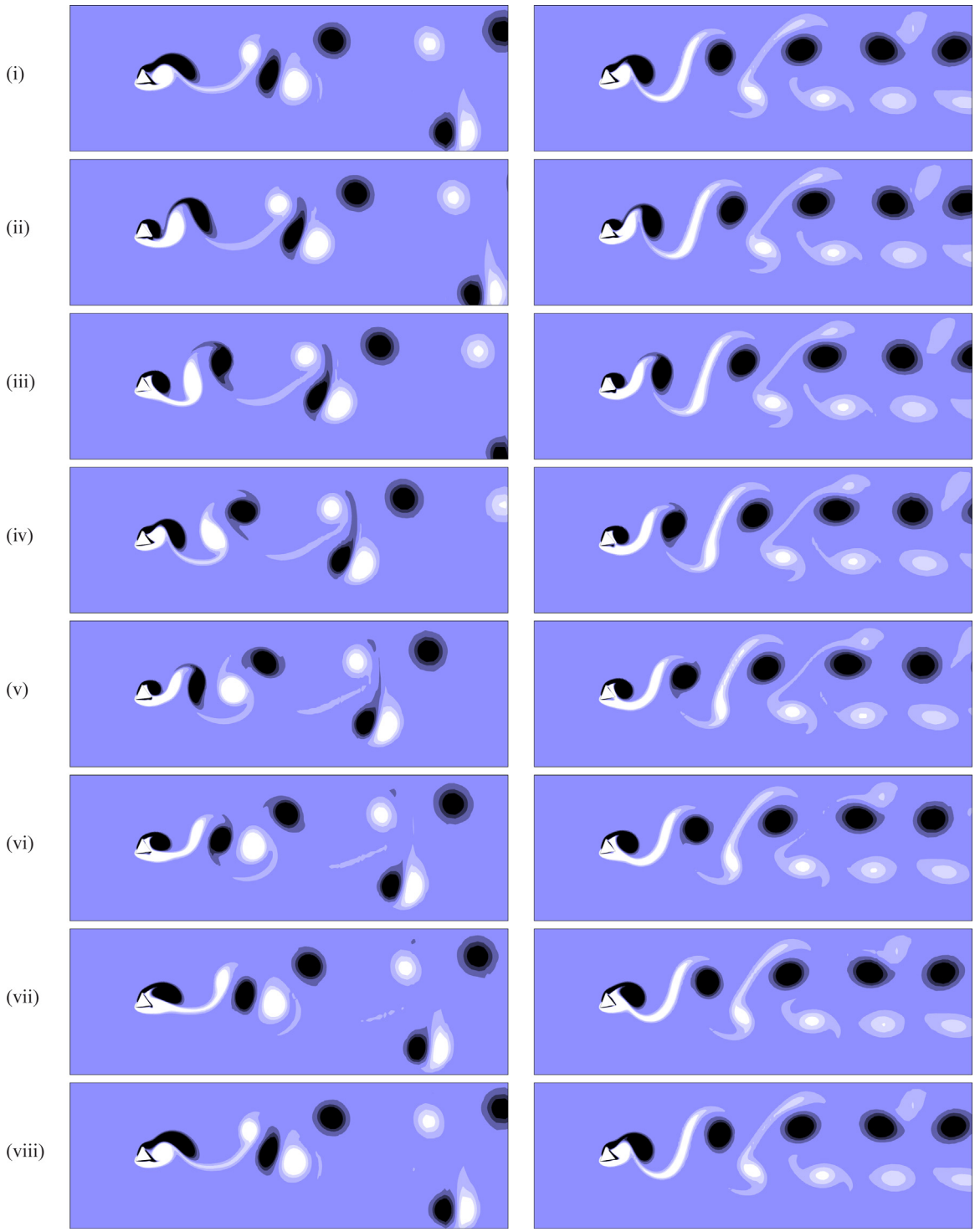

Fig. 13. Vorticity contours of the flow past the cylinder inclined at (left) $\alpha = 36^\circ$ and (right) $\alpha = 39^\circ$, both at a Reynolds number $Re=200$. The sequence of images from top to bottom describes one complete shedding cycle for the 2P-like mode (left), and the $P+S$-like mode (*right*) at 7 equi-spaced frames per cycle. Dark and light contours show negative and positive vorticities, respectively.

wake had developed a bi-layered profile shows the vortex street to first deflect away from the wake centreline before abruptly developing a multi-pair vortex street similar to the 2P wake of an oscillating cylinder (Fig. 12(left) for the cylinder inclined at $\alpha = 36^\circ$). The 2P mode in the wake of an oscillating cylinder shows a periodicity to two pairs of like-signed vortices successively shed into the wake region (Williamson and Roshko, 1988), while the 2P-like wake observed in the

present study appears to have a periodicity to two pairs of counter-rotating vortices being shed into the wake with alternate-signed vortices shed successively. The mechanism for the formation of the 2P-like mode here is similar to the vortex-interactions in the near wake that lead to the 2P mode—the development of a vortex while still attached to the body is interrupted by the developing opposite-signed vortex, leading to splitting and subsequent shedding of the older vortex (Govardhan and Williamson, 2000). For the cylinder inclined at $\alpha = 30^\circ$, the solution for the flow at $Re = 200$ describes the strongly deflected vortex street, and a quick check for the flow at $Re = 300$ showed the 2P-like wake to have developed. The shedding frequencies associated with this mode are half those of the lower Reynolds number cases, indicating periodicity of the solutions to two shed counter-rotating vortex pairs. Higher cylinder inclinations ranging over $38^\circ < \alpha \lesssim 48^\circ$ showed the vortex streets to be of a $P+S$-like mode. The $P+S$ mode observed for the oscillating circular cylinder sheds a pair of like-signed vortices and a single opposite-signed vortex into the wake per shedding cycle (Williamson and Roshko, 1988). The $P+S$-like mode takes a remarkably similar appearance to the $P+S$ mode. Most cases showing this vortex street further develops a meandering profile downstream similar to the secondary vortex street (Fig. 12(right) for the cylinder inclined at $\alpha = 42^\circ$). The meandering wake profile presumably develops for all $P+S$-like wakes (and perhaps even for the 2P-like wakes), with the downstream position of its formation exceeding the computational domain length for most cases.

Snapshots of the vorticity contours over a complete periodic cycle for the 2P-like wake (Fig. 13(left)) and $P+S$-like wake (Fig. 13(right)) reveals the interaction of the vortices to occur most intensely near the cylinder surface, affecting the vortices prior to it being shed. The effect of the asymmetric geometry is apparent—the steep streamwise inclination of the rear top-face of the cylinder presents a (sufficiently) low pressure region causing the flow over the top of the cylinder to sweep (or beat) into the wake region and interfere with the development of the positive vortex over the bottom surface of the cylinder. It appears that the factor deciding the formation of either the 2P-like wake or the $P+S$-like wake lies in the extent of the formation of the strained positive vortex on the cylinder surface (light contours in the figures) prior to an interference by the negative vortex (dark contours in the figures) sweeping into the low pressure region, and if the developing vortices interact with the intense vorticity field attached to the rear-side of the cylinder surface prior to being shed (the vortex-merging mode, VM, as mapped by Tu et al. (2014)). For the $P+S$-like wake (Fig. 13(right)), this interference occurs when the positive vortex has already formed well over the rear top-side of the cylinder prior to being shed (frame (i)) which is then wedged out into a highly strained form upon the negative vortex sweeping into the low pressure region (frames (i)–(iii), observing the vortex pair attached to the cylinder). The developing positive vortex is observed to interact with the positive vorticity field attached to the rear top-side of the cylinder (frame (v)), leading to the development of a new positive vortex (frames (v)–(viii)). After being shed from the cylinder, the strained positive vortex is further affected by the action of the adjacent negative vortex downstream causing it to split (observe the positive vortex just shed in frame (i) as it continues to stretch and eventually split by frame (viii)), thus leading to the observation of a pair of like-signed unequal-strength vortices about the single negative vortex. The 2P-like wake (Fig. 13(left)), however, shows this wedging out and straining of the positive vortex by the sweeping of the negative vortex into the low pressure region to occur only every alternate pair of counter-rotating vortices shed into the wake (frames (i)–(ii)); the other counter-rotating vortex pair shows the developing positive vortex to interact with the positive vorticity field attached to the rear top-side of the cylinder preventing the developing negative vortex from wedging the positive vortex away from the cylinder (frames (v)–(viii)), allowing the positive vortex to be shed off without as much strain introduced in its form.

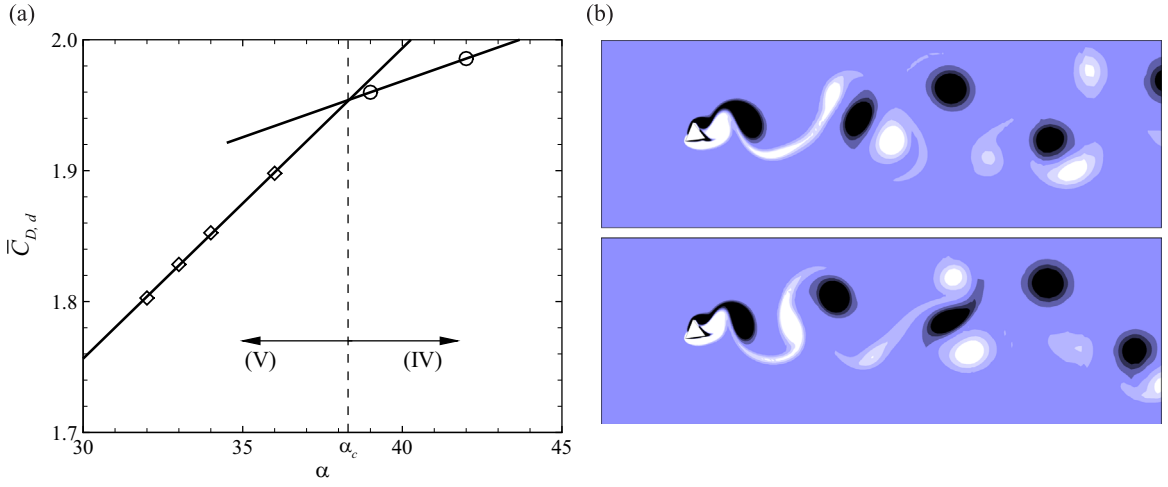

Fig. 14. (a) Plot of the time-averaged drag force coefficients, $\overline{C}_{D,d}$, against the cylinder inclination α at a Reynolds number $Re = 200$. The solid lines are linear functions—one fitted through the data for the 2P-like mode (⋄) and the other fitted through the data for the $P+S$-like mode (○), while the dashed line marks the estimated threshold between the 2P-like wake (Regime V) and the $P+S$-like wake (Regime IV). (b) Vorticity contours of the flow past the cylinder inclined at $\alpha = 38^\circ$ and at $Re = 200$ showing the wake transition from the 2P-like mode to the $P+S$-like mode, where the bottom image occurs one counter-rotating vortex-pair apart from the top image. Dark and light contours correspond to negative and positive vorticities, respectively.

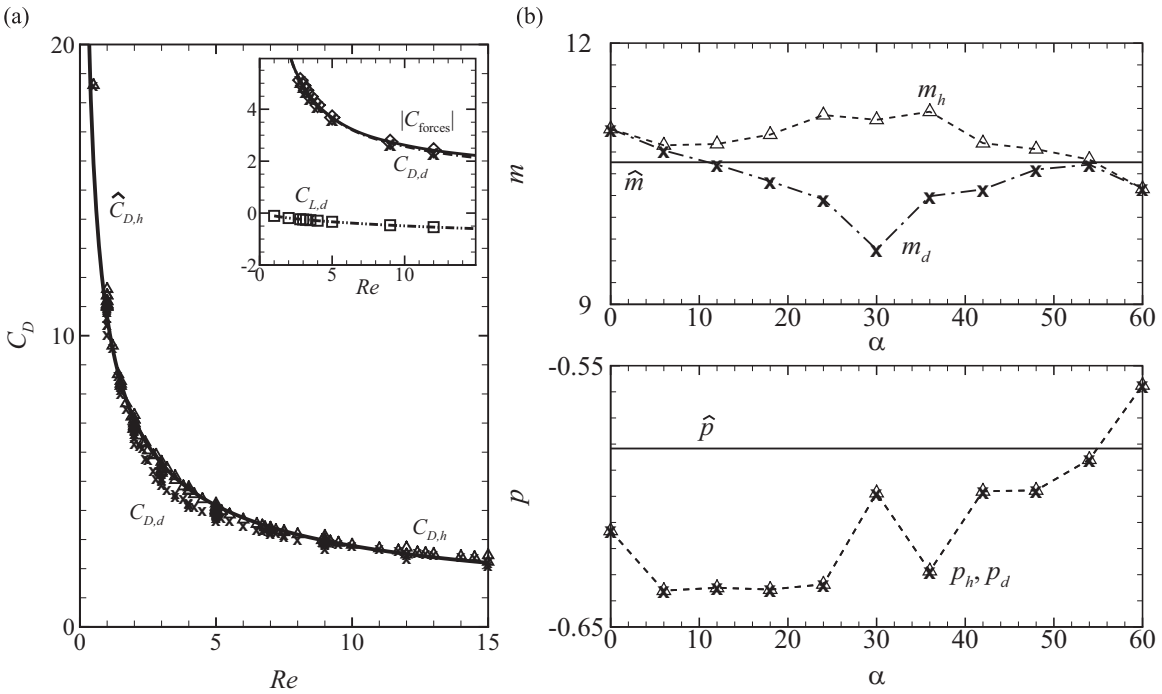

Fig. 15. (a) Plot of the drag force coefficients scaled by the projected height h (△) and by the cylinder side length d (x) against Reynolds numbers. The solid line describes the fitted function $\hat{C}_{D,h}(Re)$. (*inset*) Plot shows the drag force coefficients (x, – · line), lift force coefficients (□, – ·· line), and resultant flow-induced force coefficient (⋄, solid line) all scaled by the cylinder side length d at the low Reynolds number range when the cylinder is inclined at $\alpha = 30°$. (b) Plots of the coefficients (*top*) m, and (*bottom*) p for various cylinder inclinations α. The coefficients marked by (△) are obtained for the drag force coefficient data scaled by h, and (x) for the data scaled by d, while the solid line traversing all α marks the coefficients of the general fitted function, $\hat{m}$ and $\hat{p}$.

The transition from the 2P-like mode to the $P+S$-like mode for a flow at $Re=200$ occurs at an incidence angle of approximately 38° as predicted by a change in the trends of the drag force coefficients as shown in Fig. 14(a). At this incidence angle, a wake develops with features consistent with both modes. The vortex street initially takes a strong resemblance to the 2P-like wake, but splits the second positive vortex in the pair, which already is in a strained form, into two weaker ones. Increasing the incidence angle further presumably alters the timing of the interaction of the shedding vortices and also leads to sufficient imbalance in the vorticity distribution about the wake centreline, thereby suppressing the 2P-like form. The flow then begins to develop the $P+S$-like wake as described earlier. Extra care was taken to ensure the flows were evolved to a saturated state, precluding the possibility that the different vortex streets observed are transient features of the flow.

The authors recognise that some of the regimes mapped out in this study may be inherently three-dimensional. Numerical simulations of the 2P vortex mode in the wake of an oscillating circular cylinder by Blackburn et al. (2001) appeared three-dimensional in nature, while for the isosceles triangular cylinder with its apex pointing downstream ($\alpha = 60°$), Luo and Eng (2009) reported the flow to develop a three-dimensional instability mode consistent with the Mode A instability seen behind circular cylinders (Williamson, 1996a) beyond $Re=164$. However, the two-dimensional planes show the spanwise vortex loops to persist, agreeing with various experimental visualisations (Williamson and Roshko, 1988). As such, the 2P-like mode found in this study could perhaps be three-dimensional as well, as may several of the other regimes mapped in Fig. 10.

3.4. Flow-induced forces on the stationary cylinder

The magnitude of the forces reported in the following discussion have been scaled by the cylinder side length d to facilitate a comparison with results from Bao et al. (2010), unless specifically mentioned otherwise. At the low Reynolds number range about the onset of flow separation, the lift forces obtained were negligible relative to the drag forces induced on the cylinder (Fig. 15(a) (*inset*)). In such a laminar state and despite the asymmetry of most cylinder inclinations, the transverse momentum imbalance introduced into the flow by the cylinder is rapidly diminished, leading to the low lift force coefficients described.

The drag force coefficients induced on a circular cylinder is known to be approximately inversely proportional to low Reynolds numbers (Stokes, 1851; Oseen, 1910; Lamb, 1911). Neglecting the transverse forces (lift) induced on the cylinder, the functional relationship between the drag force coefficients and the Reynolds numbers ($Re \lesssim 15$) for various cylinder inclinations were determined in the form of $c_D = m\,Re^p$, with a plot of the drag force coefficients against the Reynolds

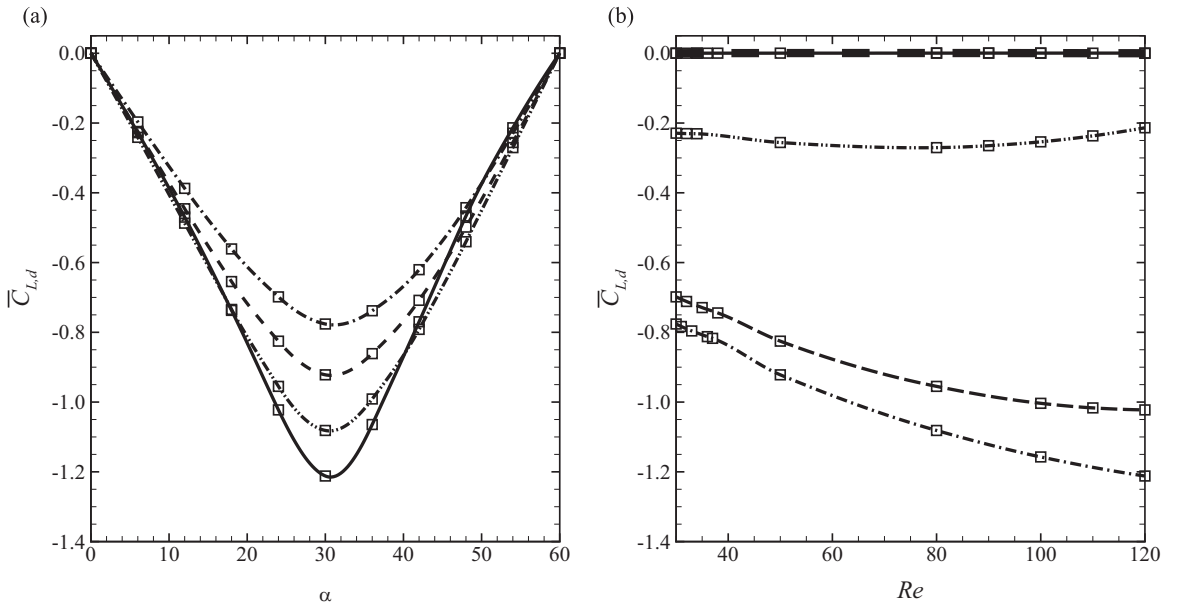

Fig. 16. Variations of the time-averaged lift force coefficient as (a) α and (b) Re are varied. In (a), lines depict $Re=30$ (– · line), $Re=50$ (– – line), $Re=80$ (–·· line) and $Re=120$ (solid line). In (b), lines are given for cylinder inclinations $\alpha = 24°$ (– – line), 30° (– · line), 54° (–·· line), and 0° and 60° (thin solid line and thick dashed line respectively, which overlap in the plot at $\overline{C}_{L,d} \approx 0$). For both plots, the data obtained are marked with □ symbols.

number being shown in Fig. 15(a). The coefficients m and p predicted for each cylinder inclination are summarised in Fig. 15(b). A similar curve fit was performed for $c_{D,h}$ against Re across all cylinder inclinations as Fig. 15(a) suggests a general form in the drag force coefficient profile for low Reynolds numbers. The general fit to the data ($\hat{c}_{D,h}$ as a function of Re) yielded the coefficients $\hat{m} = 10.6316$ and $\hat{p} = -0.5817$ (solid lines in the corresponding plots in Fig. 15(b)). Fig. 15(a) shows the fitted function (shown as a solid line) to compare well to the data obtained for the drag force coefficients (data marked by △) at these low Reynolds numbers.

The time-averaged lift force coefficients induced on the cylinder at each Reynolds number tested described a similar trend where the maximum lift force coefficient occurred at $\alpha \approx 30°$, and increases only in magnitude with the Reynolds

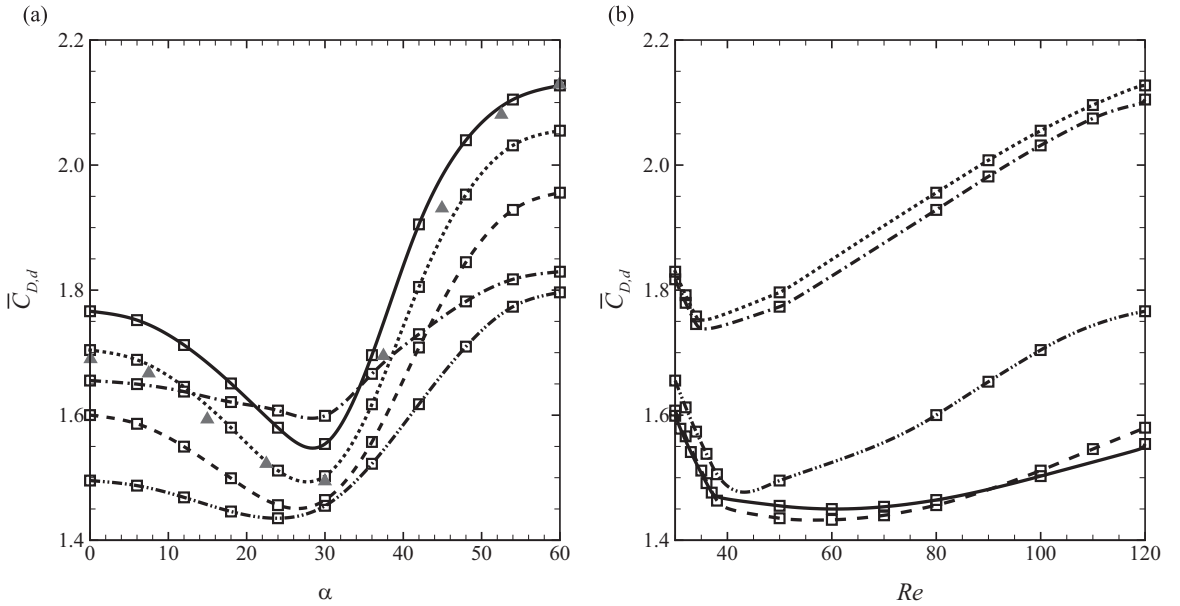

Fig. 17. Variations of the time-averaged drag force coefficient as (a) α and (b) Re are varied. In (a), lines depict $Re=30$ (– · line), $Re=50$ (–·· line), $Re=80$ (– – line), $Re=100$ (dotted line), and $Re=120$ (solid line). The (▲) symbols on the plot are results for the flow at $Re_d=100$ reported in Bao et al. (2010). In (b), lines are given for cylinder inclinations $\alpha = 0°$ (–·· line), $\alpha = 24°$ (– – line), $\alpha = 30°$ (solid line), $\alpha = 54°$ (– · line), and $\alpha = 60°$ (dotted line). For both plots, the data obtained are marked with □ symbols.

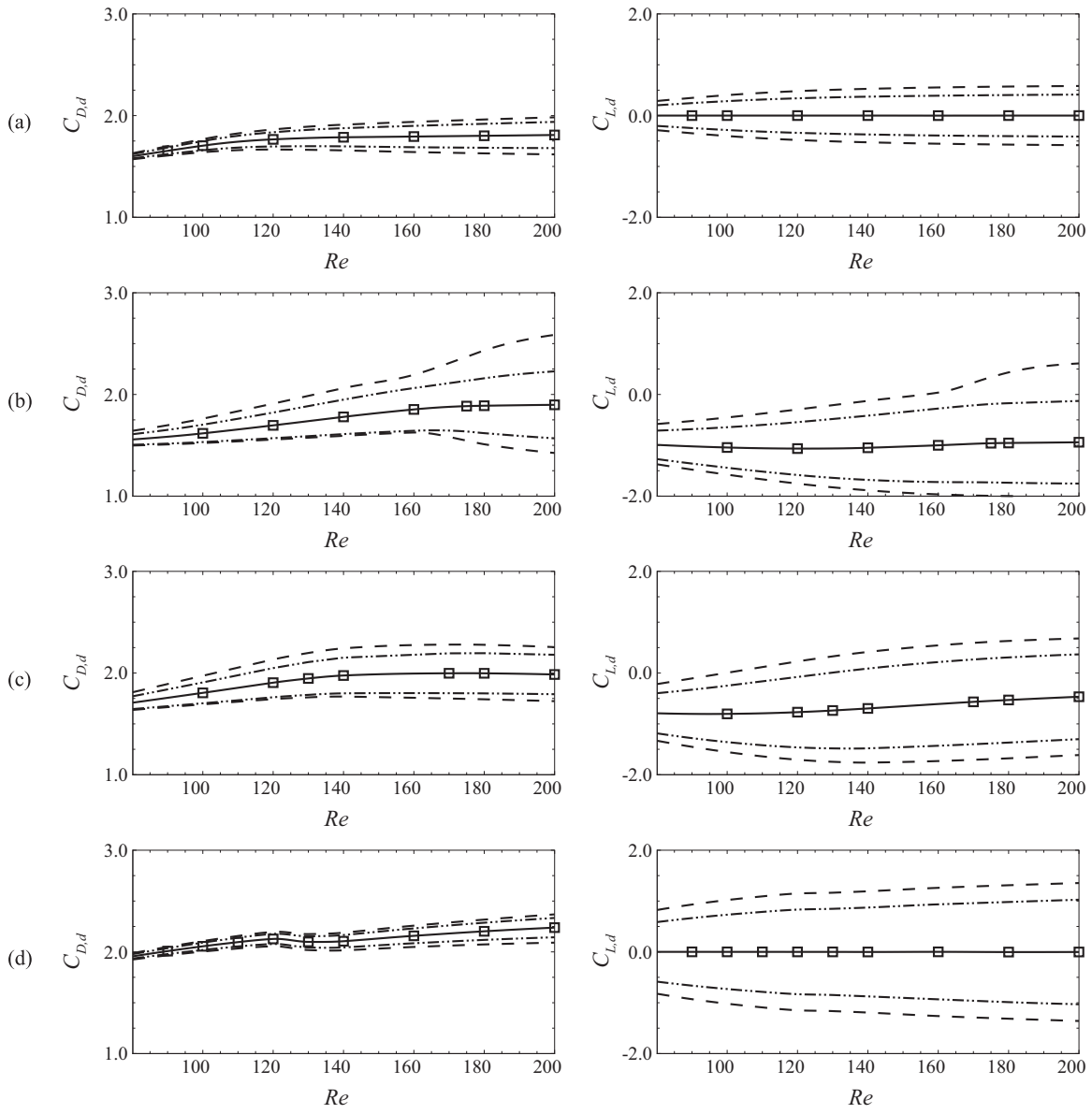

Fig. 18. Force profiles for the cylinder inclined at (a) $\alpha = 0°$, (b) $\alpha = 36°$, (c) $\alpha = 42°$, and (d) $\alpha = 60°$, with (left) showing the drag force coefficients, and (right) showing the lift force coefficients for increasing *Re*. Solid lines through the computed data (□) show the trends of the time-averaged force coefficients, (– –) lines show the fluctuation extrema, and the (⁻···) lines show the root mean square values of the fluctuations centred about the time-averaged quantity for each data point.

number (Fig. 16). As mentioned earlier, this trend relates to the cylinder inclination presenting the largest asymmetry; symmetric cylinder inclinations $\alpha = 0°$ and 60° shows a negligible time-averaged lift force coefficient value for all Reynolds numbers reported. Fig. 16(b) also shows a small change to occur in the lift force coefficient trends upon the onset of the unsteady flow regime ($Re \approx 40$ in the plot).

Fig. 17 describes the time-averaged drag force coefficient variation with both cylinder inclination and Reynolds numbers. The plot of the drag force coefficient against cylinder inclination in Fig. 17(a) shows that the drag force coefficient consistently reaches a minimum when the cylinder is inclined at approximately 30° for most Reynolds numbers, appearing consistent for both the steady-state regime (shown for $Re = 30$) as well as for the unsteady flow regimes. For all Reynolds numbers shown, the time-averaged drag force coefficients for the symmetric cylinder inclination $\alpha = 60°$ are observed to be much larger than the symmetric cylinder inclination $\alpha = 0°$. This arises from the larger wakes that are observed to develop for the cylinder inclination $\alpha = 60°$ compared to those developed for the cylinder inclined at $\alpha = 0°$. Observation of this broader wake at higher cylinder incidence angles has been reported by Iungo and Buresti (2009) for $Re_d = 1.2 \times 10^5$ flows

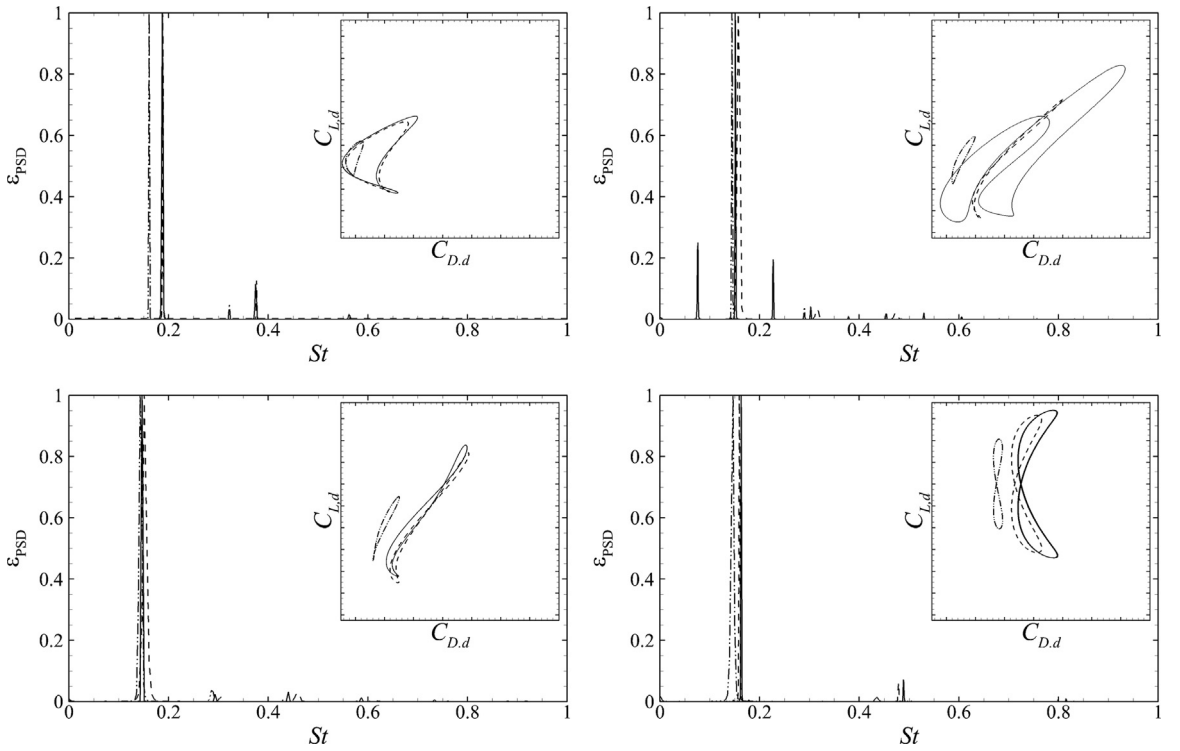

Fig. 19. Power spectral density plots showing the lift force coefficient frequency responses at Reynolds numbers Re=80 (–···), 160(– –), and 200 (solid line). Plots are shown for cylinder inclinations α = 24°, 36°, 42°, and 60° from left to right then top to bottom. Amplitudes are normalised by the peak response of each Reynolds number. (*inset*) Phase plots of the force coefficients at the corresponding cylinder inclination and Reynolds number. The plots axes are defined such that $-2.5 \le C_{L,d} \le 1.5$ and $1.5 \le C_{D,d} \le 3.0$.

past finite-span triangular cylinders. The strong dip in the trend of the drag force coefficients at the various cylinder incidence angles observed in Fig. 17(b) again relates to the transition from a steady to an unsteady flow.

Fig. 17(a) also shows the drag force coefficients reported by Bao et al. (2010) from simulations of a similar system at Re_d=100 ($86 \lesssim Re < 100$). The results from the present study compares well against the published data for cylinder inclinations $\alpha < 30°$, but shows an increasing deviation for $\alpha > 30°$ such that by $\alpha = 60°$, the results from the present study is approximately 3.5% less than the drag force coefficient predicted by Bao et al. (2010). This difference in the values predicted may possibly be due to the different computational domain size used and the boundary conditions employed—the published study utilised a smaller domain (see Section 2.2 for domain related uncertainties quantified for this study), and a towing tank boundary condition. These factors together with the fact that higher cylinder inclinations produce broader wakes which may lead to even higher domain related uncertainties provides sufficient confidence in the data obtained in the present study.

Fig. 18 describes the time-averaged force coefficients, the corresponding root mean square (r.m.s.) values about the time-averaged quantities, and the fluctuation extremes as the Reynolds number is increased for flows past the cylinder at inclinations α = 0°, 36°, 42°, and 60°. Generally, the r.m.s. values are observed to follow the trends of the time-averaged force coefficients as the Reynolds number is increased. However, this quantity fails to observe the sudden increase in the fluctuations of the force coefficients at $Re \approx 170$ for the cylinder inclined at $\alpha = 36°$ corresponding to the transition to the 2P-like wake (Fig. 18(b)). A change in the slope of the time-averaged drag force coefficient is observed at $Re \approx 110$ for the cylinder inclined at $\alpha = 0°$, $Re \approx 135$ for the cylinder inclined at $\alpha = 42°$, and $Re \approx 120$ for the cylinder inclined at $\alpha = 60°$, but these changes do not correspond to the transitions between regimes I and II (from the Bénard–von Kármán vortex street to the bi-layered wake profile) as predicted in Fig. 10. Despite mentioning earlier that the time-averaged lift force coefficients for symmetric cylinder inclinations appear negligible, the fluctuations for these cases are clearly significant, with the cylinder inclined at $\alpha = 60°$ exhibiting the largest fluctuations in the force profiles which may be detrimental to overlook.

Spectral analysis of the lift force coefficients induced on the cylinder at various Reynolds numbers (Re=80, 160, and 200) reveals the different frequency responses of the various unsteady wakes, as shown in Fig. 19. For the cylinder inclined at $\alpha = 24°$ and 60° (for the transition from the Bénard–von Kármán vortex street to the secondary vortex street), and also for the cylinder inclined at $\alpha = 42°$ (for the transition to $P+S$-like mode), the frequency responses of the lift coefficients appear highly similar through all wake regimes as expected due to the dominance of the Kármán shedding frequency in the proximity of the cylinder. It is only in the transition to the 2P-like mode, as shown for the cylinder inclined at $\alpha = 36°$, that it

exhibits multi-frequency components. At $Re=200$, the dominant frequency measured in the spectrum was again due to the Kármán shedding with $St_{BvK} = 0.151$, while the following two dominant frequencies are subharmonic with $St_1 = 0.076$ and $St_2 = 0.227$. This agrees well with the findings in Section 3.3. The phase plots shown in the inset of each spectral density plot is further evidence that only the case for the 2P-like mode transition results in a complete shift in the frequency response—all other wake regimes encountered as the Reynolds number is increased for each case shows a similar trend aside the increase in amplitudes.

4. Conclusions

The various wake regimes of two-dimensional flows past a cylinder of triangular cross-section have been described in this paper. The classical view of steady separated flows past a bluff-body having a closed 'cavity' with two symmetric recirculation bubbles is shown to be valid only for cylinder inclinations with a reflection symmetry about the horizontal centreline. Cylinder inclinations lacking this reflection symmetry (asymmetric inclinations) showed the onset of flow separation to begin with the formation of a single stationary vortex on the rear face of the cylinder, eventually developing the secondary vortex as the Reynolds number is increased but never describing a symmetric recirculation region about the wake centreline. An 'alleyway' flow feature is observed to penetrate the steady recirculation region preventing the symmetry. A simple modified length measure representative the recirculation bubble extent, the recirculation half length L_R', is proposed and validated, and then used to determine the separation Reynolds numbers, Re_s. The effect of the cylinder inclination on the separation Reynolds number is pronounced, with the value at $\alpha = 60^\circ$ being an order of magnitude higher than the separation Reynolds number for the cylinder inclined at $\alpha = 0^\circ$.

The critical Reynolds numbers for the transition to an unsteady periodic flow have also been determined using the Stuart–Landau equation. For the critical Reynolds numbers re-scaled by the cylinder side length d, the cylinder inclined at $\alpha = 28^\circ$ showed the greatest resistance to instability, while the cylinder inclined at $\alpha = 60^\circ$ was least stable. Observations of the flow in a pre-critical state (all at $Re=35$) shows the presence of a localised negative streamwise velocity bubble on the steeper upstream facing side of the cylinder at incidence angles $18^\circ \lesssim \alpha \leq 30^\circ$ to affect the stability of the steady flow strongly, while the rapid decline in the Re_c and $Re_{c,d}$ values for cylinder inclinations $34^\circ \lesssim \alpha \leq 60^\circ$ showed a rapid broadening of the wake.

For unsteady flows in the range of Reynolds numbers tested, the Bénard–von Kármán vortex street is observed to dominate the near wake for most cases. At sufficient Reynolds numbers (generally $Re \approx 100$), the shed vortices develop eccentricities in its form, which in most cases align with other like-signed vortices forming a dual-layered vorticity wake structure some distance downstream of the cylinder. Also, the position where this vortex alignment begins approaches closer to the cylinder as the Reynolds number is increased. Proceeding from this state, further increasing the Reynolds number leads to the observation of several distinct vortex streets depending on the cylinder inclination (Fig. 10). For most cases, the bi-layered wake is observed to re-arrange itself into a secondary vortex street which consists of larger vortical structures than the Bénard–von Kármán vortex street, and with it introducing incommensurability of the wake (Taneda, 1959; Durgin and Karlsson, 1971; Cimbala et al., 1988; Karasudani and Funakoshi, 1994). The cylinder inclined at $30^\circ \leq \alpha \lesssim 38^\circ$ instead developed a vortex street similar to the 2P wake of oscillating circular cylinders, while cylinder inclinations $38^\circ \lesssim \alpha \lesssim 48^\circ$ developed a $P+S$-like wake. The $P+S$-like wake further develops a meandering profile downstream similar to the secondary vortex street.

The force coefficients for the various wakes have also been quantified. The mean drag coefficient of the cylinder at various inclinations for a flow at $Re=100$ shows a good agreement with results reported by Bao et al. (2010), and the time-averaged drag and lift force coefficients show trends similar to results from wind tunnel experiments by Iungo and Buresti (2009) despite the latter study being at much higher Reynolds numbers. Transition to the 2P-like wake regime shows the fluctuations of the force coefficients to become stronger with increasing Reynolds numbers, which is not observed for the transition to the secondary vortex street and the $P+S$-like wake. The phase trajectories of the force coefficients further reflect this by showing the transition to the 2P-like mode to produce a complete shift in its profile, while the other wakes only describe increases in the force amplitudes while maintaining a similar trajectory.

The authors appreciate that the flows may possibly develop three-dimensional instabilities within the range of Reynolds numbers investigated in the present study as Luo and Eng (2009) reported for an isosceles triangular cylinder with apex pointing downstream. The stability of the two-dimensional flows at other cylinder inclinations is still unknown, but has been shown to vary at different incidence angles (Sheard et al., 2009). The onset of the three-dimensional instability across the range of cylinder inclinations may be an interesting direction for a future study.

Acknowledgements

Z.Y.N. is supported by a Faculty of Engineering International Postgraduate Research Scholarship (FEIPRS) from the Faculty of Engineering, Monash University. This research was supported by ARC Discovery grants DP120100153 and DP150102920, and was undertaken with the assistance of resources from the National Computational Infrastructure (NCI), which is supported by the Australian Government.

References

Agrwal, N., Dutta, S., Gandhi, B.K., 2016. Experimental investigation of flow field behind triangular prisms at intermediate Reynolds number with different apex angles. Exp. Thermal Fluid Sci. 72, 97–111.

Bao, Y., Zhou, D., Zhao, Y.-J., 2010. A two-step Taylor-characteristic-based Galerkin method for incompressible flows and its application to flow over triangular cylinder with different incidence angles. Int. J. Numer. Meth. Fluids 62 (11), 1181–1208.

Bénard, H., 1908. Formation de centres de giration à l'arrière d'un obstacle en mouvement. C. R. Acad. Sci. Paris 147, 839–842.

Berger, E., Wille, R., 1972. Periodic flow phenomena. Annu. Rev. Fluid Mech. 4 (1), 313–340.

Blackburn, H.M., Govardhan, R.N., Williamson, C.H.K., 2001. A complementary numerical and physical investigation of vortex-induced vibration. J. Fluids Struct. 15, 481–488.

Blackburn, H.M., Sherwin, S.J., 2004. Formulation of a Galerkin spectral element-Fourier method for three-dimensional incompressible flows in cylindrical geometries. J. Comput. Phys. 197 (2), 759–778.

Chatterjee, D., Mondal, B., 2015. Mixed convection heat transfer from an equilateral triangular cylinder in cross flow at low Reynolds numbers. Heat Transf. Eng. 36 (1), 123–133.

Cimbala, J.M., Nagib, H.M., Roshko, A., 1988. Large structure in the far wakes of two-dimensional bluff bodies. J. Fluid Mech. 190, 265–298.

De, A.K., Dalal, A., 2006. Numerical simulation of unconfined flow past a triangular cylinder. Int. J. Numer. Methods Fluids 52 (7), 801–821.

Durgin, W.W., Karlsson, S.K.F., 1971. On the phenomenon of vortex street breakdown. J. Fluid Mech. 48 (3), 507–527.

Ganga Prasath, S., Sudharsan, M., Vinodh Kumar, V., Diwakar, S.V., Sundararajan, T., Tiwari, S., 2014. Effects of aspect ratio and orientation on the wake characteristics of low Reynolds number flow over a triangular prism. J. Fluids Struct. 46, 59–76.

Govardhan, R., Williamson, C.H.K., 2000. Modes of vortex formation and frequency response of a freely vibrating cylinder. J. Fluid Mech. 420, 85–130.

Hamid, A.H.A., Hussam, W.K., Pothérat, A., Sheard, G.J., 2015. Spatial evolution of a quasi-two-dimensional Kármán vortex street subjected to a strong uniform magnetic field. Phys. Fluids 27 (5), 053602.

Hussam, W.K., Thompson, M.C., Sheard, G.J., 2011. Dynamics and heat transfer in a quasi-two-dimensional MHD flow past a circular cylinder in a duct at high Hartmann number. Int. J. Heat Mass Transf. 54 (5–6), 1091–1100.

Iungo, G.V., Buresti, G., 2009. Experimental investigation on the aerodynamic loads and wake flow features of low aspect-ratio triangular prisms at different wind directions. J. Fluids Struct. 25 (7), 1119–1135.

Jackson, C.P., 1987. A finite-element study of the onset of vortex shedding in flow past variously shaped bodies. J. Fluid Mech. 182, 23–45.

Johnson, S.A., C., T.M., Hourigan, K., 2004. Predicted low frequency structures in the wake of elliptical cylinders. Eur. J. Mech. B-Fluid. 23 (1), 229–239.

Karasudani, T., Funakoshi, M., 1994. Evolution of a vortex street in the far wake of a cylinder. Fluid Dyn. Res. 14 (6), 331–352.

Karniadakis, G.E., Israeli, M., Orszag, S.A., 1991. High-order splitting methods for the incompressible Navier–Stokes equations. J. Comput. Phys. 97 (2), 414–443.

Karniadakis, G.E., Triantafyllou, G.S., 1992. Three-dimensional dynamics and transition to turbulence in the wake of bluff objects. J. Fluid Mech. 238, 1–30.

Kumar, B., Mittal, S., 2006. Effect of blockage on critical parameters for flow past a circular cylinder. Int. J. Numer. Methods Fluids 50 (8), 987–1001.

Kumar, B., Mittal, S., 2012. On the origin of the secondary vortex street. J. Fluid Mech. 711, 641–666.

Lamb, H., 1911. On the uniform motion of a sphere through a viscous fluid. Phil. Mag. 21 (121), 112–121.

Lange, C.F., Durst, F., Breuer, M., 1998. Momentum and heat transfer from cylinders in laminar crossflow at $10^{-4} \leq re \leq 200$. Int. J. Heat Mass Transf. 41 (22), 3409–3430.

Luo, S.C., Eng, G.R.C., 2009. Discontinuities in the S-Re relations of trapezoidal and triangular cylinders. In: Proceeding of the SPIE 7522, Fourth International Conference on Experimental Mechanics, vol. 7522. Singapore, pp.75221B-1–75221B-10. http://dx.doi.org/ 10.1117/12.851461.

Mathis, C., Provansal, M., Boyer, L., 1984. The Benard-Von Karman instability: an experimental study near the threshold. J. Phys. Lett. 45 (10), 483–491.

Oseen, C.W., 1910. Über die stoke'sche formel und über eine verwandte aufgabe in der hydrodynamik. Ark. Mat. Astr. Fys. 6 (29), 1–20.

Park, J.K., Park, S.O., Hyun, J.M., 1989. Flow regimes of unsteady laminar flow past a slender elliptic cylinder at incidence. Int. J. Heat Fluid Flow 10 (4), 311–317.

Paul, I., Prakash, K.A., Vengadesan, S., 2014. Onset of laminar separation and vortex shedding in flow past unconfined elliptic cylinders. Phys. Fluids 26 (2), 023601.

Perry, A.E., Chong, M.S., Lim, T.T., 1982. The vortex-shedding process behind two-dimensional bluff bodies. J. Fluid Mech. 116, 77–90.

Posdziech, O., Grundmann, R., 2007. A systematic approach to the numerical calculation of fundamental quantities of the two-dimensional flow over a circular cylinder. J. Fluids Struct. 23 (3), 479–499.

Prhashanna, A., Sahu, A.K., Chhabra, R.P., 2011. Flow of power-law fluids past an equilateral triangular cylinder: momentum and heat transfer characteristics. Int. J. Thermal Sci. 50 (10), 2027–2041.

Provansal, M., Mathis, C., Boyer, L., 1987. Bénard-von Kármán instability: transient and forced regimes. J. Fluid Mech. 182, 1–22.

Sen, S., Mittal, S., Biswas, G., 2009. Steady separated flow past a circular cylinder at low Reynolds numbers. J. Fluid Mech. 620, 89–119.

Sen, S., Mittal, S., Biswas, G., 2011. Flow past a square cylinder at low Reynolds numbers. Int. J. Numer. Methods Fluids 67 (9), 1160–1174.

Sheard, G.J., 2011. Wake stability features behind a square cylinder: focus on small incidence angles. J. Fluids Struct. 27 (5–6), 734–742.

Sheard, G.J., Fitzgerald, M.J., Ryan, K., 2009. Cylinders with square cross-section: wake instabilities with incidence angle variation. J. Fluid Mech. 630, 43–69.

Sheard, G.J., Thompson, M.C., Hourigan, K., 2003. From spheres to circular cylinders: the stability and flow structures of bluff ring wakes. J. Fluid Mech. 492, 147–180.

Sheard, G.J., Thompson, M.C., Hourigan, K., 2004. From spheres to circular cylinder: non-axisymmetric transitions in the flow past rings. J. Fluid Mech. 506, 45–78.

Sohankar, A., Norberg, C., Davidson, L., 1998. Low-Reynolds-number flow around a square cylinder at incidence: study of blockage, onset of vortex shedding and outlet boundary condition. Int. J. Numer. Methods Fluids 26 (1), 39–56.

Sreenivasan, K.R., Strykowski, P.J., Olinger, D.J., 1987. Hopf bifurcation, Landau equation, and vortex shedding behind circular cylinders. In: Ghia, K.N. (Ed.), Proceedings of the Forum on Unsteady Flow Separation, vol. 52. , American Society of Mechanical Engineers, pp. 1–13.

Stokes, G.G., 1851. On the effect of the internal friction of fluids on the motion of pendulums. Trans. Camb. Phil. Soc. 9, 8–106.

Taneda, S., 1956. Experimental investigation of the wakes behind cylinders and plates at low Reynolds numbers. J. Phys. Soc. Jpn. 11 (3), 302–307.

Taneda, S., 1959. Downstream development of the wakes behind cylinders. J. Phys. Soc. Jpn. 14 (6), 843–848.

Thompson, M.C., Le Gal, P., 2004. The Stuart–Landau model applied to wake transition revisited. Eur. J. Mech. B-Fluids 23 (1), 219–228.

Thompson, M.C., Radi, A., Rao, A., Sheridan, J., Hourigan, K., 2014. Low-Reynolds-number wakes of elliptical cylinders: from the circular cylinder to the normal flat plate. J. Fluid Mech. 751, 570–600.

Tu, J., Zhou, D., Bao, Y., Han, Z., Li, R., 2014. Flow characteristics and flow-induced forces of a stationary and rotating triangular cylinder with different incidence angles at low Reynolds numbers. J. Fluids Struct. 45, 107–123.

von Kármán, T., 1911. Über den mechanismus des widerstandes, den ein bewegter körper in einer flüssigkeit erfährt. Göttingen Nach. Math. Phys. Kl. 23, 509–517.

Vorobieff, P., Georgiev, D., Ingber, M.S., 2002. Onset of the second wake: dependence on the Reynolds number. Phys. Fluids 14 (7), L53–L54.

Wang, H., Zhao, D., Yang, W., Yu, G., 2015. Numerical investigation on flow-induced vibration of a triangular cylinder at a low Reynolds number. Fluid Dyn. Res. 47, 015501.

Williamson, C.H.K., 1988. The existence of two stages in the transition to three-dimensionality of a cylinder wake. Phys. Fluids 31 (11), 3165–3168.

Williamson, C.H.K., 1996a. Mode A secondary instability in wake transition. Phys. Fluids 8 (6), 1680–1682.

Williamson, C.H.K., 1996b. Three-dimensional wake transition. J. Fluid Mech. 328, 345–407.

Williamson, C.H.K., 1996c. Vortex dynamics in the cylinder wake. Annu. Rev. Fluid Mech. 28 (1), 477–539.
Williamson, C.H.K., Roshko, A., 1988. Vortex formation in the wake of an oscillating cylinder. J. Fluids Struct. 2 (4), 355–381.
Yoon, D.-H., Yang, K.-S., Choi, C.-B., 2010. Flow past a square cylinder with an angle of incidence. Phys. Fluids 22 (4), 043603.
Zdravkovich, M.M., 1968. Smoke observations of the wake of a group of three cylinders at low Reynolds number. J. Fluid Mech. 32 (2), 339–351.
Zdravkovich, M.M., 1969. Smoke observations of the formation of a Kármán vortex street. J. Fluid Mech. 37 (3), 491–496.
Zeitoun, O., Ali, M., Nuhait, A., 2011. Convective heat transfer around a triangular cylinder in an air cross flow. Int. J. Thermal Sci. 50 (9), 1685–1697.
Zielinska, B.J.A., Wesfreid, J.E., 1995. On the spatial structure of global modes in wake flow. Phys. Fluids 7 (6), 1418–1424.